Current Sheets, Magnetic Islands, and Associated Particle Acceleration in the Solar Wind as Observed by *Ulysses* near the Ecliptic Plane

Olga Malandraki[1] , Olga Khabarova[2,17] , Roberto Bruno[3] , Gary P. Zank[4] , Gang Li[4] , Bernard Jackson[5] ,
Mario M. Bisi[6] , Antonella Greco[7] , Oreste Pezzi[8,9,10] , William Matthaeus[11] , Alexandros Chasapis Giannakopoulos[11] ,
Sergio Servidio[7], Helmi Malova[12,13] , Roman Kislov[2,13] , Frederic Effenberger[14,15] , Jakobus le Roux[4] , Yu Chen[4] ,
Qiang Hu[4] , and N. Eugene Engelbrecht[16]

[1] IAASARS, National Observatory of Athens, Penteli, Greece
[2] Heliophysical Laboratory, Pushkov Institute of Terrestrial Magnetism, Ionosphere and Radio Wave Propagation of the Russian Academy of Sciences (IZMIRAN),
Moscow, Russia; habarova@izmiran.ru
[3] Istituto di Astrofisica e Planetologia Spaziali, Istituto Nazionale di Astrofisica (IAPS-INAF), Roma, Italy
[4] Center for Space Plasma and Aeronomic Research (CSPAR) and Department of Space Science, University of Alabama in Huntsville, Huntsville, AL 35805, USA
[5] University of California, San Diego, CASS/UCSD, La Jolla, CA, USA
[6] RAL Space, United Kingdom Research and Innovation—Science & Technology Facilities Council—Rutherford Appleton Laboratory, Harwell Campus,
Oxfordshire, OX11 0QX, UK
[7] Physics Department, University of Calabria, Italy
[8] Gran Sasso Science Institute, Viale F. Crispi 7, I-67100 L'Aquila, Italy
[9] INFN/Laboratori Nazionali del Gran Sasso, Via G. Acitelli 22, I-67100 Assergi (AQ), Italy
[10] Dipartimento di Fisica, Universita' della Calabria, I-87036 Cosenza, Italy
[11] Department of Physics and Astronomy, University of Delaware, Newark, DE 19716, USA
[12] Scobeltsyn Nuclear Physics Institute of Lomonosov Moscow State University, Moscow, Russia
[13] Space Research Institute (IKI) RAS, Moscow, Russia
[14] Helmholtz Centre Potsdam, GFZ German Research Centre for Geosciences, Potsdam, Germany
[15] Bay Area Environmental Research Institute, NASA Research Park, Moffett Field, CA 94035, USA
[16] Center for Space Research, North-West University of Potchefstroom, South Africa

Abstract

Recent studies of particle acceleration in the heliosphere have revealed a new mechanism that can locally energize particles up to several MeV nucleon^{-1}. Stream–stream interactions, as well as the heliospheric current sheet (CS)—stream interactions, lead to formation of large magnetic cavities, bordered by strong CSs, which in turn produce secondary CSs and dynamical small-scale magnetic islands (SMIs) of ∼0.01 au or less owing to magnetic reconnection. It has been shown that particle acceleration or reacceleration occurs via stochastic magnetic reconnection in dynamical SMIs confined inside magnetic cavities observed at 1 au. The study links the occurrence of CSs and SMIs with characteristics of intermittent turbulence and observations of energetic particles of keV–MeV nucleon^{-1} energies at ∼5.3 au. We analyze selected samples of different plasmas observed by *Ulysses* during a widely discussed event, which was characterized by a series of high-speed streams of various origins that interacted beyond Earth's orbit in 2005 January. The interactions formed complex conglomerates of merged interplanetary coronal mass ejections, stream/corotating interaction regions, and magnetic cavities. We study properties of turbulence and associated structures of various scales. We confirm the importance of intermittent turbulence and magnetic reconnection in modulating solar energetic particle flux and even local particle acceleration. Coherent structures, including CSs and SMIs, play a significant role in the development of secondary stochastic particle acceleration, which changes the observed energetic particle flux time–intensity profiles and increases the final energy level to which energetic particles can be accelerated in the solar wind.

Key words: acceleration of particles – magnetic reconnection – solar wind – Sun: heliosphere – Sun: magnetic fields – turbulence

Supporting material: animation

1. Introduction

Energetic particles in the heliosphere and magnetosphere pose significant radiation hazards for astronauts in current and future space missions in our solar system (e.g., to Mars) and for communication satellites (e.g., Iucci et al. 2006; National Research Council 2006; Malandraki 2015; Miroshnichenko 2015; Malandraki & Crosby 2018a, 2018b). Studies of their origin and properties are very important for timely protection of onboard equipment and human resources. Protons and electrons of keV–MeV energies observed in the inner

heliosphere are known to be accelerated during solar flares and at coronal mass ejection (CME) driven shocks. In the latter case, the acceleration process is most effective in the corona. Generated energetic particles are referred to as solar energetic particles (SEPs; Reames 1999; Malandraki et al. 2012; Desai & Giacalone 2016; Malandraki & Crosby 2018a, 2018b). Another source of keV–MeV nucleon^{-1} energetic particles is stream/corotating interaction regions (SIR/sCIRs). In this case, acceleration takes place at SIR/CIR-driven shocks usually formed at 2–3 au (Malandraki et al. 2007; Tsubouchi 2014; Richardson 2018). In summary, the dominant paradigm suggests that energetic particles in the keV–MeV energy range propagate to 1 au either from the Sun or from distant sources

---
[17] Author for correspondence.

1

associated with CIRs, and thus the effect of local processes can be neglected.

The standard mechanism typically invoked to explain the energization of particles locally in the solar wind is that of diffusive shock acceleration (DSA), as shown by Lee & Ryan (1986) and Zank et al. (2000), although other mechanisms have been proposed (e.g., Fisk & Gloeckler 2012, 2014; Laurenza et al. 2016; Pallocchia et al. 2017). The basic physics were elucidated especially well in the seminal papers of Axford et al. (1982) and Bell (1978a, 1978b) in the context of the astrophysical problem of cosmic-ray acceleration at supernova remnants. However, detailed interplanetary observations are not easily interpreted in terms of the simple original steady-state models of particle acceleration at shock waves. Three fundamental aspects make the interplanetary problem more complicated than the typical astrophysical problem: the time dependence of the acceleration and the solar wind background, the geometry of the shock, and the long mean free path for particle transport away from the shock. Consequently, the shock itself introduces a multiplicity of timescales, ranging from shock propagation timescales to particle acceleration timescales at parallel and perpendicular shocks. Many of these timescales feed into other timescales—these can determine maximum particle energy scalings or escape timescales, for example, from which accelerated particle distribution functions are predicted that can be broken power laws or power laws with exponential rollovers in velocity space.

Models describing the acceleration of ions at CME-driven shocks have become increasingly sophisticated and capable of explaining many observations associated with gradual events (Zank et al. 2000; Rice et al. 2003; Li et al. 2003; Verkhoglyadova et al. 2015). Only relatively low-energy energetic particles tend to remain localized near the shock where DSA occurs. These spectra, at least in the low-energy regimes, are predicted by the original and the most recent DSA models (Zank et al. 2000) to exhibit an exponential rise in intensity for a given energy ahead of the shock and then to be constant downstream of the shock.

Despite the success of the coupling of DSA to CME-driven shocks in explaining many SEP observations, numerous examples of energetic particle events simply cannot be accounted for by DSA, especially those that exhibit characteristics of obviously local acceleration or intensity profiles that possess features that suggest additional acceleration processes. For example, sometimes energetic particle flux enhancements are observed further than several correlation lengths downstream of a shock, i.e., too far to allow accelerated particles coming back to the shock front to be reaccelerated again (see, e.g., Zank et al. 2015a, 2015b; 2018). Recent simulations confirm the ability of dynamical colliding small-scale magnetic islands (SMIs) to contribute to local particle acceleration (Guo et al. 2016a, 2016b; Du et al. 2018). Furthermore, time–intensity profiles of the energetic particle flux often do not correspond to predictions for a pure DSA case, as reflected in the behavior of a so-called amplification factor exceeding 1 downstream of the shock front instead of reaching the predicted "1" plateau. We discussed such events in Zank et al. 2015a, 2015b, Khabarova et al. (2015a, 2016), Khabarova et al. (2017, 2018), and Khabarova & Zank (2017).

Very often the interpretation of observations of energetic ions at lower energies up to 1–2 MeV faces great problems, as higher-energy ion flux time–intensity profiles behave in accordance with expectations of SEP observations at 1 au, but keV–MeV energy ion flux shows variations, increases, and time delays corresponding to propagation of some solar wind structures (see Khabarova et al. 2015a and references therein).

The role of DSA in local particle acceleration has been found not to be of primary importance in many events. Khabarova & Zank (2017) illustrated how to distinguish between effects of local DSA and particle energization associated with another local source, which can be more effective, just through the visual inspection of time–intensity profiles of the energetic particle flux in different energy channels (e.g., see their Figure 12). Khabarova & Zank (2017) carried out an extensive analysis of particle energization in the vicinity of reconnecting exhausts observed in the supersonic solar wind by the *ACE* spacecraft. Both the case study analysis and the superposed epoch analysis of 126 reconnection exhaust events, which mainly occurred within interplanetary coronal mass ejections (ICMEs), showed that energetic ions are accelerated up to at least 5 MeV and electrons up to 0.315 MeV within a time interval of ±30 hr around reconnecting current sheets (CSs). Khabarova & Zank (2017) concluded that the observed long-timescale atypical energetic particle event (AEPE) encompassing the reconnection exhausts is very likely related to secondary reacceleration of energetic particles in SMIs or medium-scale magnetic islands surrounding the reconnecting CSs. Their results are in a very good agreement with predictions based on a theory of stochastic particle energization in the supersonic solar wind via numerous dynamically interacting small-scale flux ropes (Zank et al. 2014, 2015a, 2015b; le Roux et al. 2015, 2016, 2018a, 2018b). Initial particle acceleration may occur in different ways, including acceleration at interplanetary shocks combined with reconnection at CSs.

Reconnecting small-scale CSs are observed very often within ICMEs (see, e.g., Xu et al. 2011), which means that a magnetic cloud (MC) can be significantly twisted or fragmented (or both), as both observations and modeling show (Fermo et al. 2014; Khabarova et al. 2016; Khabarova & Zank 2017; Manchester & Van Der Holst 2017). The distortion of an MC and the simultaneous formation of SMIs can result from ICME interactions with other large-scale streams and flows, as well as from ICME propagation through the turbulent solar wind (Antiochos et al. 2011).

As an ICME propagates farther from the corona, more and more SMIs are produced by magnetic reconnection at CSs that separate fragmented larger-scale flux ropes. As a result, in situ measurements at 1 au often reveal the coexistence of both larger- and smaller-scale magnetic islands and flux ropes instead of a simply shaped MC. Observations show that some ICMEs are disconnected from the coronal source almost from the beginning of their propagation through the solar wind (DeForest et al. 2012), and others are detached from the Sun at larger heliocentric distances, especially in the case of the ICME interaction with other streams. The latter can be seen in heliospheric images of ICMEs from the Solar Mass Ejection Imager (SMEI) and interplanetary scintillation (IPS) tomography (e.g., Jackson et al. 2004, 2006, 2008, 2009; Bisi et al. 2008; Bisi 2016, and references therein) and the *STEREO* heliospheric imagers. Owing to the formation of strong CSs (SCSs) at ICME edges, magnetic islands within an ICME become isolated very quickly from the surrounding solar wind by SCSs, and the development of local acceleration processes may occur.

Coherent structures are known to energize particles, or at least to initiate particle acceleration. Khabarova et al. (2015a, 2015b, 2016, 2017, 2018) found that puzzling or atypical energetic particle flux enhancements of a doubtful origin, AEPEs, occur in magnetically confined regions that contain SMIs with a typical width of ~0.01 au or less. Either the heliospheric current sheet (HCS) or SCSs of various origins that have equally strong background magnetic fields provide the magnetic confinement of SMIs that experience dynamical merging or contraction. A new mechanism that can energize particles up to several MeV nucleon^{-1} locally in the solar wind has been introduced by Zank et al. (2014, 2015a, 2015b) and developed by le Roux et al. (2015, 2016, 2018a, 2018b). The idea that particle acceleration is associated with the dynamics of SMIs has a long history, rooted primarily in simulations (Matthaeus et al. 1984; Ambrosiano et al. 1988; Dmitruk et al. 2004; Drake et al. 2006, 2010, 2013; Pritchett 2008; Oka et al. 2010; Guo et al. 2012; Bian & Kontar 2013; Dalena et al. 2014). The purely theoretical approach suggests various possibilities for particle acceleration by dynamic magnetic islands and CSs, which includes first- and second-order Fermi mechanisms and energization by antireconnection electric fields (Zank et al. 2014, 2015a; le Roux et al. 2015, 2016, 2018a).

Observations show the occurrence of puzzling energetic particle flux enhancements that are not easily interpreted by classical DSA models of particle acceleration and transport in the heliosphere (Malandraki et al. 2005, 2008; Mulligan et al. 2008; Al-Sawad et al. 2009; von Rosenvinge et al. 2009; Chollet et al. 2010; Foullon et al. 2011; Stasiewicz et al. 2013; Zharkova & Khabarova 2015; Tessein et al. 2016). We call them "unusual, puzzling," or "atypical" energetic particle events (AEPEs) in terms of their poor correspondence to the dominant paradigm that energetic particles of keV–MeV energies come either from the corona or from shocks, with no suggestion of other possible local sources of accelerated particles. The most frequently used explanation for the inconsistency between expectations and observations is that it is due to the abrupt loss of connection to the distant source of accelerated particles. However, the number of puzzling events is too large to be simply an exception from the rule. Indeed, there are some signatures of the association of the events discussed in the list of publications cited above with local dynamic processes. Some of them were reanalyzed and interpreted with a new approach in our recent publications (Khabarova et al. 2015a, 2015b, 2016, 2017, 2018; Khabarova & Zank 2017), and some of the events will be discussed in the future.

Observational signatures of AEPEs are as follows: AEPEs observed at timescales from ~1/2 hr to several hours, sometimes against a background of SEP events, and very often in the relatively quiet solar wind, near the HCS. The latter unambiguously points to a local source of energetic particles as they are observed by well-separated spacecraft with a time delay, corresponding to the propagation of a particular solar wind structure from one s/c to another. This feature is common for all unusual/atypical events. Furthermore, velocity dispersion spectrograms (so-called 1/ion speed spectrograms) for heavy ions show a signature of local particle acceleration, i.e., a vertical pattern usually characteristic for local DSA at interplanetary shocks in front of ICMEs but without any shocks observed within several correlation lengths around an

event (Khabarova & Zank 2017). Therefore, some short-term time–intensity variations are very likely associated with crossings of local particle acceleration regions embedded in the background solar wind, and a possibility of local effects should never be excluded.

The numerous mismatches between the predictions of the dominant DSA paradigm and in situ observations may be due to the simplified approach, which assumes that energetic particles propagate almost freely in open configurations of the interplanetary magnetic field (IMF) within one to several astronomical units. However, SCSs like the HCS affect the spatial distribution of SEPs (Battarbee et al. 2017). SCSs are also formed at the edges of streams. Stream–stream interactions, as well as the interaction of different streams and the HCS, create complex configurations of magnetic boundaries in the heliosphere. Since streams of various origins often coexist in the solar wind, magnetic cavities can be formed (Khabarova et al. 2016, 2017, 2018). The latter are usually filled with coherent structures produced by magnetic reconnection at their borders.

Numerical simulations help understand many features of magnetic-island coalescence and the behavior of particles accelerated in dynamical processes in magnetic islands that might occur in the heliosphere. For example, with simulations it is easy to see the evolution of a "sea" of differently sized magnetic islands, separated by CSs, as well as the process of particle trapping and acceleration produced by turbulence (Servidio et al. 2009, 2010, 2011, 2015; Valentini et al. 2016; Pucci et al. 2017; Pezzi et al. 2018). This confirms the ideas on a close link between turbulence, magnetic reconnection, and formation of coherent structures (Marsch 2006; Sahraoui et al. 2007; Alexandrova et al. 2008; Gary et al. 2010; Bruno & Carbone 2013).

Observational evidence for particle acceleration by reconnection-associated processes has been controversial in the solar wind (Gosling et al. 2005; Khabarova & Zank 2017), unlike observations in Earth's magnetosheath, where particle energization by SMIs appears to be quite well accepted. Magnetic reconnection is intrinsic to and a natural consequence of the nonlinear cascade process in a magnetofluid (e.g., Servidio et al. 2009, 2010, 2011; Lazarian et al. 2012). Whether in the context of tearing-mode-driven reconnection or in the context of MHD turbulence, neighboring islands of the same chirality can be attracted to one another by the Lorentz force. This process is quite similar to coalescence of magnetic flux ropes observed in laboratory plasmas (Furno et al. 2005; Gekelman et al. 2012, 2016, 2018). In the latter case, magnetic flux ropes are formed as the result of the developing twist and collision of elongated magnetized laser-created plasma beams with distance from the source over time, revealing striking similarities to flux rope formation and coalescence in the solar corona.

Wherever flux ropes of a cross-section size approximately one order smaller than a typical ICME MC size are created, they experience numerous twists, instabilities, and further magnetic reconnection that reconfigures and tears them up as they are advected with the solar wind. The same process of fragmentation of elongated flux ropes or magnetic tubes and the formation of isolated magnetic islands and numerous CSs is observed in laboratory plasma (Gekelman et al. 2012, 2016, 2018). As a result, well-separated magnetic islands are formed during the flux rope interaction and magnetic reconnection. In turn, magnetic islands also evolve and experience merging,

contraction, and oscillations. As noted above, magnetic islands in the corona and the solar wind are produced during magnetic reconnection at SCSs. Consequently, at a certain distance from the Sun, spacecraft can observe magnetic islands of both coronal and local origin. Large-scale heliospheric structures, such as the rippled HCS or SIRs/CIRs, can bound regions occupied by a "sea" of magnetic islands. Considering the creation of SMIs and CSs during the magnetic reconnection and downstream of interplanetary shocks as an essential manifestation of turbulence, one can infer a strong linkage between characteristics of turbulence, coherent structures like CSs and SMIs, and the effects of local particle acceleration in the heliosphere (Gonzalez et al. 2017).

There are numerous theory and simulation papers (Guo et al. 2014, 2015, 2016a, 2016b; Zank et al. 2014, 2015a; le Roux et al. 2016, 2018a, 2018b; Li et al. 2017, 2018a, 2018b), as well as observational papers (Khabarova et al. 2015a, 2015b, 2016; Khabarova & Zank 2017; Zhao et al. 2018, Adhikari et al. 2019), supporting in detail the mechanism of particle energization by processes occurring in dynamical magnetic islands as a particle acceleration process, which is discussed in this paper. The overwhelming majority of AEPEs have been detected at 1 au. As noted above, observations at larger distances suggest that particle transport and energization in the heliosphere are even more complicated than offered by the dominant paradigm. Zhao et al. (2018) have recently reported *Ulysses* observations of an energetic particle flux enhancement event downstream of a shock near 5 au that is inconsistent with the predictions of classical DSA but may be explained by local acceleration associated with SMIs. Zank et al. (2015a) show that the energetic particle intensity profile observed by *Voyager* 2 downstream of the heliospheric termination shock (84 au) appears to support a particle acceleration mechanism that combines both DSA and magnetic-island-reconnection-related processes.

Any speculations on a possible origin of ICME-associated AEPEs should involve ISs since most ICMEs drive forward shocks in front of them. As mentioned above, unusual (or atypical) energetic particle flux enhancements are often detected in the region far downstream of an IS. The region corresponds to the main body of an ICME, i.e., an MC. It is quite obvious that a freely expanding MC cannot produce any particle acceleration inside the cloud. However, as mentioned above, there are cases of AEPEs observed within ICMEs, which are associated with deflected and sometimes detached ICMEs with highly twisted and fragmented MCs that become transformed into a series of relatively large SMIs during the propagation of an ICME from the Sun to a spacecraft. The latter makes the theory by Zank et al. (2014, 2015a) applicable to the case. The event that we discuss below is of this sort. We will show that there are signatures of simultaneously acting different mechanisms of particle acceleration within the complex ICME structure discussed by Malandraki et al. (2007).

In this work, we use the stream–stream interaction event identified by Malandraki et al. (2007) observed by *Ulysses* at ∼5.3 au in the ecliptic plane to illustrate that the occurrence of local coherent structures, namely, magnetic islands and small-scale CSs separating them in a confined region, can lead to the development of additional particle acceleration, which impacts time–intensity profiles of the energetic particle fluxes substantially.

2. Methods

A complete understanding of an ICME-associated AEPE is impossible without considering the multiscale processes that occur as an ICME propagates through the solar wind plasma full of simultaneously occurring large-scale structures such as HCS, CIRs, and other ICMEs. Processes and structures created by turbulence should be taken into account as well. To understand the event at both large and small scales, we will analyze first its solar sources with *Solar and Heliospheric Observatory* (*SOHO*) imagery, using the Helioviewer facilities (see https://helioviewer.org/) and a "Computer Aided CME Tracking" software package (CACTUS): http://sidc.oma.be/cactus/).

The way an ICME propagates determines the occurrence or not of AEPEs, since this depends on details of ICME deflection, the detaching and formation of fragmented MCs, secondary flux ropes, magnetic islands, and magnetic cavities. As shown in our previous work (Khabarova et al. 2015a, 2015b, 2016, 2017, 2018), the interplanetary imagery is an excellent tool to understand key features of the propagation of a particular ICME. The reconstructed 3D density plots are based on SMEI data (http://smei.ucsd.edu/new_smei/index.html). SMEI operated from 2003 to 2011, which covers the time interval of interest. SMEI (Eyles et al. 2003; Jackson et al. 2004) was designed to image nearly the entire sky in visual light during each 102 minutes of Earth orbit in Thomson-scattered visible/white light. SMEI was the first true heliospheric imaging system to track CMEs outward from the Sun until they arrive at Earth (Jackson et al. 2004; Tappin et al. 2004). The photometric signals from SMEI allow time-dependent 3D reconstructions of density and modeled 2D images from these (e.g., Jackson et al. 2006, 2008, 2009; Bisi et al. 2008; Buffington et al. 2008, 2009; Bisi 2016).

In the 3D tomographic reconstructions from SMEI, the brightness values that determine density are often combined with solar wind velocities and from observations of IPS. These were usually available over the same interval from the Institute for Space-Earth Environmental Research (ISEE), Nagoya University Japan, to help define the large-scale flow of heliospheric structures. However, during the SMEI era, ISEE (formerly STEL/STELab) was unable to operate in winter months, and so in this investigation we will rely on the SMEI brightness information alone to provide the 3D reconstructions. We will use the reconstructions from the SMEI data to illustrate that at least two CMEs observed by *Ulysses* at 5.2 au almost merged on their way from the Sun to Earth and were overtaken by a superfast third ICME at greater distances, as discussed in Malandraki et al. (2007).

To link the large- and small-scale processes that took place in the complex CIR-ICME system, we employ two methods to identify coherent structures: the PVI method (Greco et al. 2018) and the direct identification of CSs as suggested by Li (2008).

The method called "Partial Variance of Increments" (PVI) has been increasingly used in analysis of spacecraft and numerical simulation data since its inception in 2008. The purpose of the method is to study the kinematics and formation of coherent structures in space plasmas. The PVI technique is intended to be a simple, easily implemented methodology. Indeed in its basic form, PVI is applied to a one-dimensional signal, such as a time series obtained in a high-speed flow, as would be seen by a single spacecraft in the solar wind, or by a fixed probe in a wind tunnel. PVI is essentially a time series of the magnitude of a vector increment with a selected time lag,

normalized by its average over a selected period of time. As such it depends on three parameters—its cadence, the time lag, and the interval of averaging (see Greco et al. 2018, for details). It is a "thresholding" method, and once a threshold has been fixed on PVI signal, a collection or hierarchy of "events" can be identified. It has been shown that the probability distribution of the PVI statistic derived from a non-Gaussian turbulent signal strongly deviates from the probability density function of PVI computed from a Gaussian signal, for values of PVI greater than about 3. As PVI increases to values of 4 or more, the recorded "events" are extremely likely to be associated with coherent structures and therefore inconsistent with a signal having random phases. Thus, as threshold is increased, stronger and rarer events are identified, associated with highly non-Gaussian coherent structures. The method is intended to be quite neutral regarding the issue of what mechanism generates the coherent structures it detects. Indeed, the method is sensitive to directional changes, magnitude changes, and any form of sharp gradient in the vector magnetic field B. The PVI quantity is not biased toward a particular type of discontinuity (directional, tangential, and rotational discontinuities and shocks) or other structures. The necessary literature on various applications of the method can be found in Greco et al. (2018).

The direct method of the identification of CSs calculates the angle between two magnetic field vectors measured at a time separation of tau and examines how this angle changes as a function of tau. The details of the method can be found in Li (2008). The essence of the method is the following: when a thin CS is present with the time interval tau, one expects to find an elevated angle for a period of tau. Increasing the separation time from tau to 2 tau, the duration for observing an elevated angle also increases to 2 tau. One can therefore identify the location of the CS, as well as its thickness. Because the method makes use of different time lags, it is less affected by measurement anomalies. Using this method, Miao et al. (2011) have examined multiyear data from *Ulysses* observations and obtained various statistics of CSs in the solar wind at different heliocentric distances. Li et al. (2011) used this method to identify 24 hr periods that are most and least populated by CSs using *ACE* data for over 10 yr. They then showed that the property of solar wind magnetic field turbulence spectra depends on the presence of CSs.

Both the PVI and CS identification methods can be used to visualize the level of turbulence and the formation of coherent structures. At the same time, these methods are distinct and cannot replace each other since they are meant to identify different structures. The PVI method shows all possible coherent structures, only some of which are CSs. In combination, the methods allow us to analyze the properties of coherent structures in solar wind plasma of different kinds. For example, one can calculate the number of CSs and the number of high PVI events (considering different thresholds) to find how these characteristics vary in solar wind of different origins.

We furthermore present a classical analysis of the characteristics of turbulence including Alfvénicity and spectra to study the similarities and differences between solar wind from different sources and understand what regimes are more favorable for local particle acceleration. Since we have found that the occurrence of energetic particle flux enhancements of a presumably combined origin is associated with the presence of magnetic islands, we also employ the Grad–Shafranov (GS) technique to reconstruct SMIs observed within the periods of

interest. A description of the technique and its applications in plasma physics can be found in Sonnerup & Guo (1996), Hau & Sonnerup (1999), Hu (2017), Chen et al. (2018), and Zhao et al. (2018).

Time–intensity profiles of the energetic particle flux will be compared with the IMF characteristics and the presence of coherent structures. Additionally, to distinguish between single-event DSA and a combination of DSA and the magnetic-island-associated mechanism of particle acceleration, we will use both the spatial energy separation method and an "amplification factor" method as described and previously demonstrated by Zank et al. (2015a) and Khabarova & Zank (2017). Zank et al. (2015a) find that a combination of classical diffusive shock acceleration and further downstream acceleration in a sea of dynamical magnetic islands can explain the observed energetic ion flux profiles. Classical DSA predicts a peaking of the particle intensity of a given energy at the shock, after which it is constant, which automatically makes the amplification factor equal to 1 downstream of the shock. However, the particle intensity, when normalized by the intensity measured at the shock, is clearly not 1 in many events. The "amplification factor" property for extra acceleration downstream of the shock emerges from the solution proposed by Zank et al. (2014) (see their Equation (39)). One can plot the spatial profile of the solution at different energies (see Figure 5 of Zank et al. 2014 and Figure 13 of Zank et al. 2015a), and the plots can be normalized to the value of the intensity measured at a boundary. The particle intensity amplification for a particular particle energy is predicted by Equation (39) from Zank et al. (2014) (i) to increase with increasing energy and (ii) to exceed the "1" level characteristic for a pure DSA case. For example, Figure 12 of Khabarova et al. (2016) shows the amplification factor for the combined DSA–magnetic-island case, and Figure 13 of Khabarova & Zank (2017) shows solutions of Equation (39) from Zank et al. (2014) illustrating the amplification factor and spatial distribution of particles in the absence of other particle acceleration sources besides dynamical magnetic islands. In summary, if the flux amplification factor peaks at the shock and then remains nearly constant or decreases, this is most probably the DSA case, but if the flux amplification increases far downstream of an IS, some other downstream mechanisms of particle energization are almost certainly involved, and the examination of the IMF properties for the presence of magnetic islands should be performed. In our experience, there was no case when the flux amplification increase was observed well behind an IS without the occurrence of magnetic islands.

3. Observations and Data Analysis

3.1. Solar Sources of 2005 January Events, Propagation and Interaction of the Streams in the Interplanetary Medium

The behavior of the Sun was very complex during the period of interest, as discussed in Malandraki et al. (2007). Figures 1(a) and (b) show the coexistence of active regions and huge coronal holes, one of which extended to low heliolatitudes. The northern coronal hole served as a source of a long-lived CIR that interacted with all ICMEs ejected toward Earth. One may combine this with an analysis of corresponding CACTUS maps of the locations of the CMEs (http://sidc.oma.be/cactus/catalog/LASCO/2_5_0/2005/01/latestCMEs.html), in which the excitation of interconnected eruptions in a belt across the
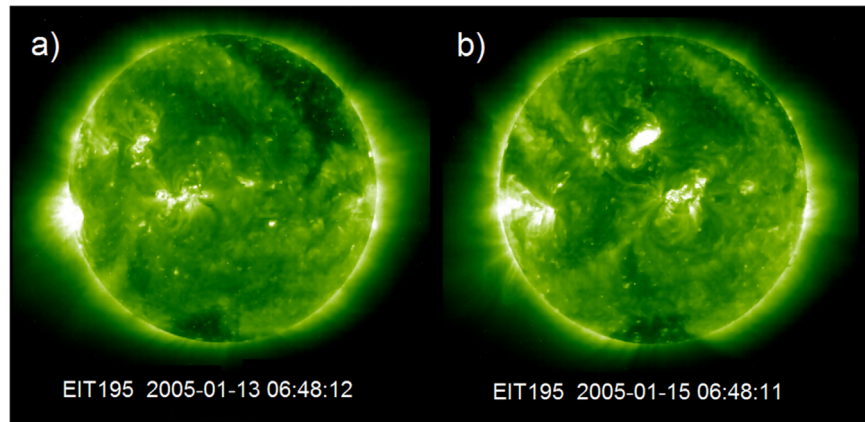
Figure 1. Example of solar sources of the streams observed by *Ulysses* in 2005 January. LASCO EIT 195A images (a) 2 days before and (b) on the date of the first halo CME eruption, 2005 January 15. Active regions coexist with a coronal hole that reaches low latitudes.

Sun, sometimes occurring with a small time shift and resulting series of halo CMEs observed in 2005 January 15–22, is seen. The corresponding multiwavelength movie from LASCO coronagraphs 2 and 3 can be found on the official LASCO EIT webpage: http://www.ias.u-psud.fr/eit/movies/movies/195/eit195-200501-512-lz.mpeg, http://www.ias.u-psud.fr/eit/movies/movies/284/eit284-200501-512-lz.mpeg.

Energetic particle observations in the 3.8–19 MeV energy range, as measured by the COSPIN/LET instrument onboard *Ulysses*, following the intense solar activity in 2005 January, were presented and discussed by Malandraki et al. (2007) (see Figure 2). Malandraki et al. (2007) found that the ICME transient material observed by *Ulysses* on days 29–39, 2005 (shown by a horizontal solid bar in Figure 2), was due to *Ulysses* being in a favorable position (see Figure 3 of Malandraki et al. 2007) to detect during this period a system of solar wind transient flows that resulted from the interaction and coalescence of a series of unusually fast halo CMEs ejected from the Sun during 2005 January 15–20, in association with AR 10720, culminating with the one of the fastest halo CMEs that was ejected on January 20. The arrival time of the structure illustrated in Figure 2 was found to be consistent with the times of ejection of the fast halo CMEs at the Sun from 2005 January, 15–20. Individual transient solar wind disturbances resulting from multiple CMEs at the Sun tend to coalesce to form larger, more complex structures (e.g., Richardson et al. 2005; Jian et al. 2011) by the time they reach 5 au. If, at the same time, the background solar wind is dominated by a more or less regular pattern of fast and slow streams that form SIRs, CIRs, or some form of shear layers (e.g., Forsyth & Marsch 1999, and references therein; Gosling & Pizzo 1999; Gosling et al. 2001; Bisi et al. 2010, and references therein), the result is often the formation of so-called compound streams (e.g., Burlaga et al. 1986). Such a CME/SIR combination has been also measured by *Ulysses* at similar heliocentric distances during the 2005 August/September period, which was also during the declining phase of the solar cycle 23, where CIRs/SIRs are predominantly observed in the heliosphere (Malandraki et al. 2008). Multiple shocks are often seen in association with the passage of such ICME/SIR combinations at such heliocentric distances (Burlaga et al. 1986; Malandraki et al. 2007, 2008). In 2005 January, three forward shocks (indicated by the red vertical lines in Figure 2) and a later reverse shock were observed in association with the ICME/CIR interaction.
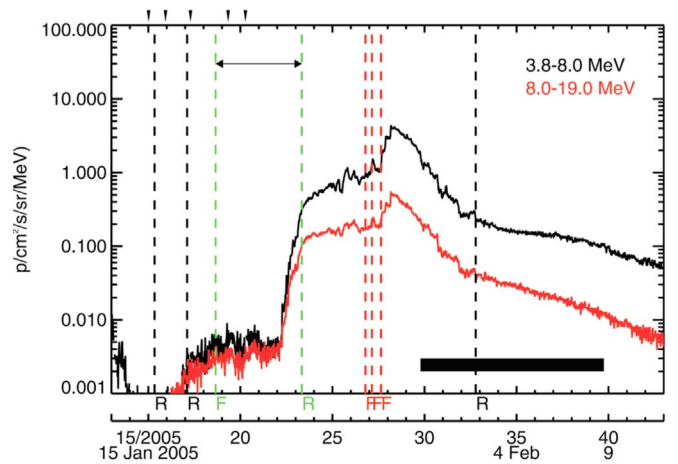

Figure 2. Energetic proton intensity profiles are shown in two energy channels in the range 3.8–19 MeV as measured by the COSPIN/LET telescope onboard *Ulysses*, during the period from days 13 to 43, 2005. Solid vertical lines mark the time of occurrence of forward (F) and reverse (R) shocks. F shocks in red indicate ICME-driven shocks, whereas the green vertical lines represent the F and R shocks that bound a CIR. Black downward-pointing triangles denote the times of X-class flares. A CME/CIR combination is observed by *Ulysses* at 5.2 au during this period, resulting from the coalescence of individual transient flows generated by a series of solar events in 2005 January, interacting with the preexisting pattern of CIRs (see text) (adapted from Malandraki et al. 2007).

As was shown by Malandraki et al. (2007), energetic particles (1.8–19 MeV) injected from the Sun during the 2005 January period of intense solar activity were not observed at *Ulysses* until a stream interface (associated with a preceding CIR that is indicated by the green vertical lines in Figure 2) that acted as a barrier to the particles reached the spacecraft (see Figure 4 of Malandraki et al. 2007). They concluded that, at least at the energies measured by LET, the energetic particle profiles observed by *Ulysses* at 5 au during this interval do not show evidence for direct propagation from the Sun to the observer but appear to be controlled by large-scale solar wind structures crossing the spacecraft.

The evolution of the first two CMEs, which have linear speeds of 2049 and 2547 km s^{-1} (https://cdaw.gsfc.nasa.gov/CME_list/), through the inner heliosphere further from the Sun can be traced at least approximately with 3D SMEI density reconstructions, and these are demonstrated in Figure 3. Earth's position, indicated by the blue circle, is fixed in the series of panels shown in Figure 3(a). The coronal hole flow appears as
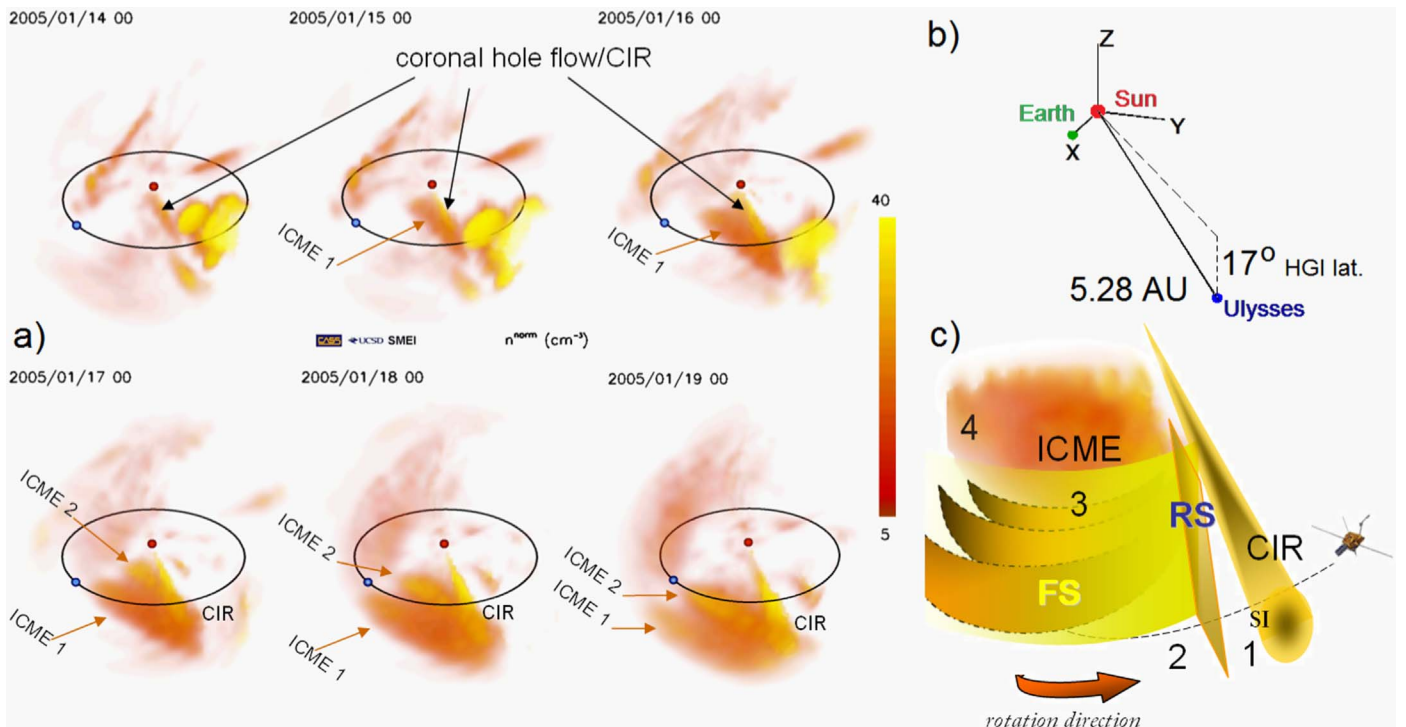
Figure 3. Stream propagation and interaction in the interplanetary medium. (a) Example of SMEI observations of the solar wind density between Earth (blue circle) and the Sun (red circle) in 2005 January. The long-lived coronal hole seen almost at the equator in Figure 5(a) is the source of a stable flow that becomes a CIR. The CIR represents a wall that can deflect and deform ICMEs. An animation of panel (a) is available. The video begins at 2005 January 14, 00:00 UT and ends at 2005 January 19, 00:00 UT. The video duration is 12 s. (b) *Ulysses* position with respect to Earth. (c) Resulting configuration of streams and interplanetary shocks at 5.2 au. Since the entire system rotates sunwise, *Ulysses* subsequently observes the CIR, the stream interface (SI), the reverse shock (RS) of the CIR, the ICME-driven forward shocks (FS), and finally the merged ICME.

(An animation of this figure is available.)

an elongated quasi-stable cone slowly rotating anticlockwise. In this background, two ICMEs appear in interplanetary space. Because of the prior CIR, they cannot propagate freely, being deflected by the CIR and forced to propagate not just radially but rotating with the CIR. Since the two ICMEs have different speeds and propagate in a complicated way, their fronts merge to arrive at Earth's orbit as a complex fast-stream region. We illustrate here that a series of several shocks can be observed successively even at 1 au since each ICME is preceded by a shock, and if ICMEs merge on their way to Earth, the shocks may be observed one by one. Further, the steepening and merging of shocks occur, and the resulting structure sometimes may appear at 3–5 au as one shock of a split form (i.e., Jian et al. 2008, 2011).

As seen in Figure 2, *Ulysses* observed the three not completely merged interplanetary shocks. The third, i.e., the fastest ICME on 2005 January 20 with a speed of 3242 km s^{-1} when the CME first appeared in the LASCO field of view (Gopalswamy et al. 2012), which is not shown in Figure 3(a), interacted with the ICME conglomerate shown in Figure 3(a) at larger heliocentric distances and merged with the previous two. Unfortunately, this process is not visible through SMEI reconstructions, as the frame does not cover larger distances. An alternative way to infer it using ENLIL is also unavailable, as ENLIL does not have an archive for 2005.

However, understanding the way streams propagate (Malandraki et al. 2007) and knowing *Ulysses*' position with respect to Earth (Figure 3(b)), it is possible to reconstruct a sequence of events to determine the large-scale picture of the stream profiles observed by *Ulysses*. The sketch shown in

Figure 3(c) illustrates a plausible scenario suggested from in situ observations and prior reconstructions of the ICME paths. Figure 3(c) shows the sequence in which the key regions of the CIR and the complex ICME were crossed by *Ulysses* at 5.28 au. The entire picture rotates from the left to the right. As a result, *Ulysses*, which practically stands still with respect to the propagating and rotating solar wind, crosses the corresponding structures from left to right. Its virtual path through the structures is shown by a dotted line. The CIR appears as a cone; its reverse shock RS separated from the CIR stream interface with region 1 is shown as a vertical boundary (although in reality it has a shape of the CIR). Region 2 in front of the merged ICME is supposed to be relatively quiet, encompassing/carrying no CIR or ICME material. After that, *Ulysses* subsequently enters the FS shock conglomerate and the ICME merged sheath (region 3) and the main ICME body, consisting of remnants of ICME flux ropes (region 4).

3.2. Ulysses *Observations at* ~5.3 au

3.2.1. Variations in the IMF and Plasma Parameters and Corresponding Energetic Particle Flux Enhancements

The in situ counterpart of the interplanetary situation illustrated in Figure 3(c) is shown in Figure 4, as observed by *Ulysses* at 5.28–5.27 au between days 22 and 31 of 2005. From top to bottom we show average values, computed on a 1 hr scale, starting from the original data that we resampled with a sampling time of 8 minutes. Shown from top to bottom are total pressure P_T (magnetic plus kinetic), proton temperature T_P, solar wind speed V, proton number density ρ, and
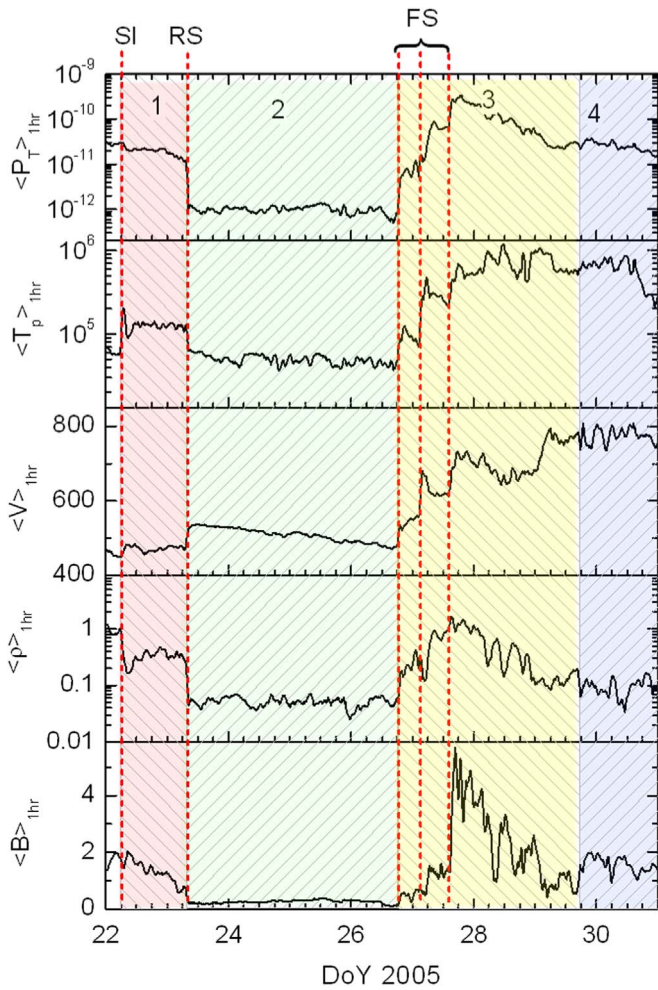
Figure 4. From top to bottom: 1 hr average values of the total pressure P_T in dyne cm^{-2}, T^{large} in degrees, the speed in km s^{-1}, the proton number density in 1 cm^{-3}, and the magnetic field intensity in nT, respectively.
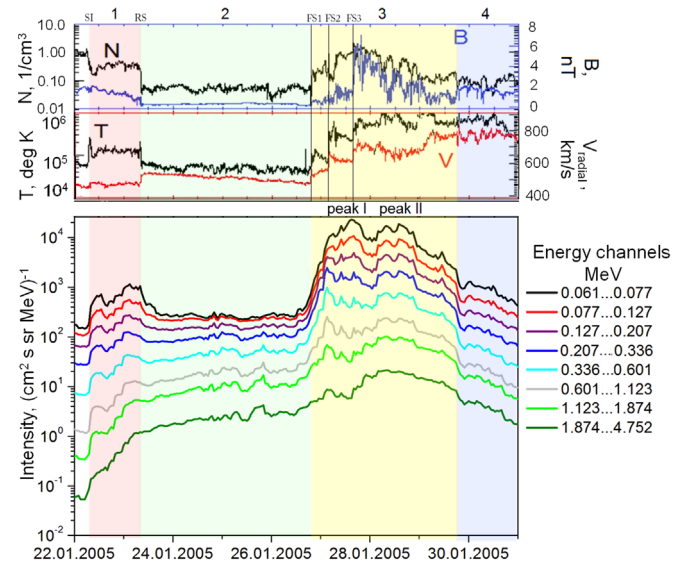

Figure 5. Variations in the solar wind plasma and IMF parameters and impact of local plasma/IMF configurations on energetic ion flux profiles. From top to bottom: the solar wind density (black) and the IMF strength (blue), the solar wind temperature (black) and the solar wind speed (red), and LEMS120 measurements of energetic ion flux in corresponding energy channels. Forward shocks of the merged ICME are shown by vertical lines FS1–FS3.

magnetic field intensity B. Vertical dashed lines indicate, from left to right, the location of the stream interface (SI), the reverse shock (RS), and the three ICME-driven forward shocks FS, corresponding to the sketch of Figure 3(c). SI is the Stream Interface of the CIR bounded by the two green dashed vertical lines in Figure 2.

Different shading throughout the data identifies the different regions preceding and following the ICME. These regions are easily identified by the behavior of the parameters shown in the various panels. From a simple inspection of these parameters it clearly results that regions 1, 2, and 4 are characterized by the presence of pressure-balanced structures, as shown by the constant value of the total pressure in the top panel.

Therefore, according to the plasma and IMF observations of *Ulysses* (Figure 4), the four regions shown in Figure 3(c) can be identified as follows:

First (the interval between SI and RS): from 2005 January 22, 06:50 UT to 2005 January 23, 08:20 UT;

Second (a quiet interval between the CIR and the ICME, from the RS to the first of the three FSs): from 2005 January 23, 08:20 UT to 2005 January 26, 19:06:23 UT;

Third (an ICME merged sheath): from 2005 January 26 19:06:23 UT to 2005 January 29 18:00:00 UT; and

Fourth (an ICME main body): from 2005 January 29 18:00:00 to 2005 January 31 00:00:00 UT.

The forward shock positions are as follows: 2005 January 26, 19:06:23 UT (shock 1); 2005 January 27, 03:25:51 UT (shock 2), and 2005 January 27, 15:28:12 UT (shock 3). The shocks possess rather similar characteristics and can be considered as quasi-parallel, as their θ_{Bn} angle (the angle between the normal vector and the magnetic field direction upstream of the shock) is 37°, 46°, and 37° respectively (see the shock database and the method of calculation at http://ipshocks.fi/database).

To illustrate the behavior of the energetic ion flux, we use measurements of the LEMS120 detector of the HI-SCALE experiment onboard *Ulysses* (Lanzerotti et al. 1992), since the lower-energy channels of the LEMS30 detector were contaminated during the corresponding period (Marhavilas et al. 2015). It should be noted that the inspection shows that despite this effect, the time–intensity profiles of LEMS30 and LEMS120 are very similar in all energy channels (not shown). A detailed analysis of high-resolution IMF/plasma data and hourly energetic ion flux from the LEMS120 telescope reveals the existence of two main peaks of the energetic ion flux in energies up to 1 MeV observed during the period of interest: the smaller double peak associated with CIR region 1 and the higher double peak observed within region 3 (see Figure 5). The feature of Figure 5 that draws the most attention is that lower-energy energetic ions behave almost independently of higher-energy particles (compare the black and green curves). If SEPs propagate from a coronal source freely, time–intensity profiles of lower-energy ions should be determined strictly by the behavior of higher-energy ions. Certainly, if there are strong coherent structures or areas of strong turbulence on the way of propagating SEPs, the observed time–intensity profile may become irregular, showing dropouts and small fluctuations, especially in low-energy channels (e.g., Heras et al. 1995; Lario et al. 1998; Ng et al. 2003), but the level of the energetic particle flux usually does not change considerably,

and the averaged time–intensity profiles of lower-energy particles still follow the higher ones. In the event discussed here, this is not the case.

A remarkably different behavior of the low-energy and high-energy particles is observed within the entire period shown in Figure 5. We will describe the features of energetic ion flux profiles, following *Ulysses'* path from right to left in the frame of the rotating solar wind shown in Figure 3(c), but from left to right in the frame of Figure 5, following the course of events observed by Ulysses. The occurrence of different regimes in the time–intensity profile behavior inside the CIR and outside of it (after the RS crossing) suggests different characteristics of propagation of the energetic particles. An abrupt enhancement of the lower-energy (0.061–0.601 MeV) ion intensities is observed at the passage of the SI over the spacecraft (see the corresponding structure in Figure 3(c)). At the passage of the RS, a more gradual decrease is observed in the lower-energy ion flux profiles, with the intensity levels getting back to nearly pre-event levels and exhibiting a plateau thereafter, within region 2.

Energetic ions of higher-energy intensities (from 0.601 to 4.752 MeV), as observed in regions 1 and 2, have typical SEP characteristic profiles in a similar way to that shown in Malandraki et al. (2007). Since particles of such energies can penetrate any shock freely, an abrupt increase in the higher-energy energetic ion flux begins in association with the SI crossing. This is consistent with the IMF/plasma configuration shown in Figure 3(c). The RS expands from the right to the left practically perpendicular to open magnetic field lines in front of the ICME in region 2. Calculations show that the θ_{Bn} angle of the shock was 79°. Both the RS and SI represent two plasma/ IMF barriers for SEPs. It is known that energetic particles of different energies are differently sensitive to the presence of magnetic barriers, i.e., some particles can cross a barrier, but the others can be stopped and deflected at it. SEPs injected during the 2005 January solar events and propagating ahead of the merged ICME cannot penetrate into the main CIR area, which looks like an increase at the SI in the higher-energy ion flux in Figure 5. Sometimes, CIR-associated RSs accelerate particles up to several MeV, but the particular RS does not possess a necessary properties and is unable to accelerate particles to high energies locally. The RS does not impact high-energy ion flux time–intensity profiles since no clear changes in them are seen at energies above 1 MeV. As a result, following their abrupt onset, the corresponding curves continue to increase uninterruptedly, smoothly, and gradually in region 2.

Energetic electron flux time–intensity profiles behave very similarly to those of high-energy ions, being insensitive up to the RS position but increasing after its passage (not shown). According to Zank et al. (2014, 2015a), electrons are affected by the acceleration mechanism as well, but they have much smaller gyroradii than ions, which makes them more mobile. As a result, energetic electron flux time–intensity profiles usually do not show obvious small-scale variations, while a spacecraft crosses magnetic islands and CSs separating magnetic islands in the region of particle acceleration. Instead, energetic electrons form a cloud of accelerated particles around the entire area where the acceleration takes place, and it is not easy to visually extract a smoothly elevated level of the electron flux from the background level of solar or DSA origin. We discussed this phenomenon in our previous papers, especially in Khabarova & Zank (2017).
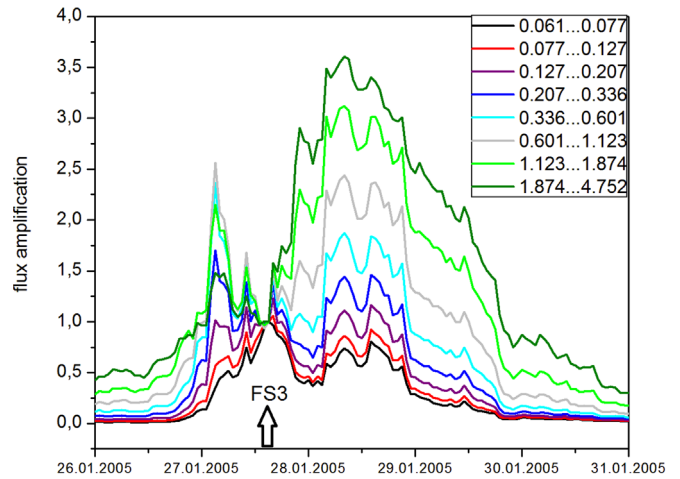

Figure 6. Amplification factor calculated with respect to the position of the third forward shock.

The substantial difference between high- and low-energy ion flux profiles observed in region 1 can be explained by the fact that the RS shock is transparent for high-energy particles, whereas low-energy particles cannot leak through the RS. The SI acts as a barrier for both lower- and higher-energy particles, so the energetic ion flux profiles at all energies show an enhancement only after the time of its crossing. However, the intensity profiles of the low- and high-energy ions exhibit a prominently different behavior. The enhancements observed in low energies are CIR associated with a possible impact of DSA at the RS, but at the same time, they are quite possibly determined by the existence of magnetic islands inside region 1, as typical DSA-associated profiles always peak at the shock position.

Summarizing, lower-energy ion flux enhancements observed in region 1 are definitely not related to the SEP propagation. These particle enhancements are not totally due to the RS either, because there are two peaks within the region and none of those are observed to have a maximum coinciding with the shock position. Energetic particles of lower energies shown in Figure 5 apparently become accelerated inside region 1 by different and independent mechanisms, one of which is of a local origin (also see the Discussion). It is evident that there are energy channels in which both DSA and Zank's mechanisms operate (based on observations of the humps in 0.336–1.123 MeV channels).

If energetic ions observed by *Ulysses* were only SEPs, the profile of SEP would continue to increase smoothly without additional peaks in region 3. However, evidently there could be an extra population seen in the background of the preexisting SEPs. The question arises: Are those extra peaks far down-stream of ISs related to DSA only, or there is also another origin for these energetic particle enhancements? Energetic ions with energies greater than ∼1 MeV nucleon^{-1} exhibit only one peak in region 3 as discussed previously by Malandraki et al. (2007) (see Figure 2), who showed that the peak is determined by SEPs and probably DSA at the merged shock. However, in the case of pure DSA, energetic particle flux profiles in lower-energy channels would display the same behavior as high-energy particles. Furthermore, classic DSA-associated profiles show only one maximum exactly at the shock position, either forming a sharp peak or decreasing slowly in the shock wake. In the discussed event, the strongly modulated form of the time–intensity profiles seen in Figure 5
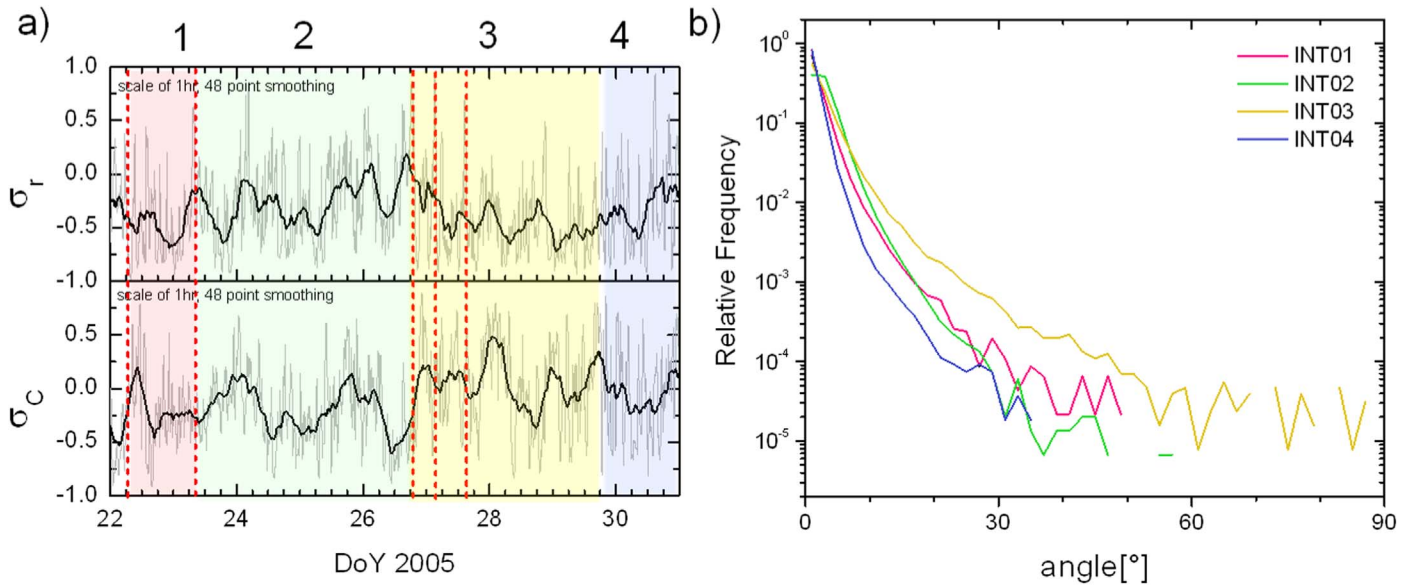
Figure 7. Alfvénicity analysis and IMF field direction changes in the four intervals. (a) Gray line: 1 hr averages of normalized residual energy σ_r (top panel) and cross-helicity σ_C (bottom panel) smoothed with a running average of length 48 hr (dark line) to guide the eye. (b) Histograms of the angle between two successive magnetic field vectors for the four different time intervals. Data sampling time is 2 s. The colors correspond to the intervals shown in panel (a).

may indicate more complex processes of particle acceleration related to local IMF/plasma structures. The positions of the peaks observed in different lower-energy channels in Figure 5 correspond to each other. Analysis of higher-time resolution data confirms this (not shown). Therefore, there is no signature of the velocity dispersion, which suggests that the source of particle acceleration is local (please find the corresponding explanations on the velocity dispersion in Khabarova & Zank 2017).

Interestingly, the low-energy ion flux varies at the three shocks significantly (in the peak I area indicated in Figure 5), but the time–intensity profiles of high-energy ions do not show any noticeable variations in the vicinity of FS1–FS3. This means that DSA is ineffective at higher energies, and region 3 is filled with particles belonging to different populations in terms of their origin. Lowest-energy particles that are sensitive to local structures are presumably energized by dynamic processes in magnetic islands and also related to DSA occurring at the three shocks. Highest-energy particles are predominantly SEPs. Note that both DSA and SEP populations may serve as seed particles for dynamical magnetic islands.

From a detailed analysis, one can find that the peaks in energetic ion flux in channels 0.061–1.874 MeV are determined by local coherent structures in the solar wind. The top panel of Figure 5 shows a clear anticorrelation between the density and the IMF strength that is present in regions 1 and 3 but not in regions 2 and 4. The anticorrelated pulses of N and B are especially well pronounced in region 3. This is one of the signatures for the occurrence of magnetic islands (Cartwright & Moldwin 2010; Khabarova et al. 2015a). Other signatures will be discussed in the next section. Here we stress the fact that the key to understanding the strange behavior of lower-energy ions in regions 1 and 3 is an association with local IMF/plasma structures. The peaks in channels 0.061–1.874 MeV in region 1 are found to correspond to crossings of CSs separating magnetic islands. The same correspondence is found between the occurrence of CSs and the modulated energetic ion time–intensity profiles in region 3.

The fact that energetic ion flux enhancements observed within the ICME sheath (region 3) have various origins can be proved through an analysis of Figure 6 that shows the flux amplification calculated for the eight energy channels. The zero-point that is shown by the arrow corresponds to the last shock (FS3) position. In the case of pure DSA, the flux amplification should be 1 downstream of the shock. The existence of a prominent peak far behind the shock is a signature of some unaccounted-for processes that accelerate particles occurring within the ICME sheath. At the same time, the order of the curves with higher energies on the top is a signature of the particle acceleration mechanism proposed by Zank et al. (2014) that suggests energization of charged energetic ions by dynamical magnetic islands. Specifically, the mechanism shows that energetic particles with larger gyroradii are trapped and accelerated in magnetic islands more efficiently. Simple modulation of time–intensity profiles by small-scale coherent structures could not provide such a steady flux amplification, as the related effect would be intermittent and not continuous. Therefore, the second peak in energetic particle flux enhancements observed within region 3 (peak II in Figure 5) is presumably a result of local dynamical processes. Additionally, SEPs may be trapped and reaccelerated.

The results illustrated in Figures 5 and 6 allow us to conclude that coherent structures in the solar wind not only modulate the energetic ion flux time–intensity profiles (see, e.g., Trenchi et al. 2013) but also contribute to local particle acceleration. To study the differences and similarities between the four regions separated by plasma-magnetic barriers, we carry out an analysis of IMF variations below in terms of properties of turbulence and typical characteristics of magnetic islands.

3.2.2. Turbulence and Coherent Structures

The main goal of this section is that of corroborating the idea that local coherent structures effectively contribute to particle acceleration in the heliosphere. As already discussed in the
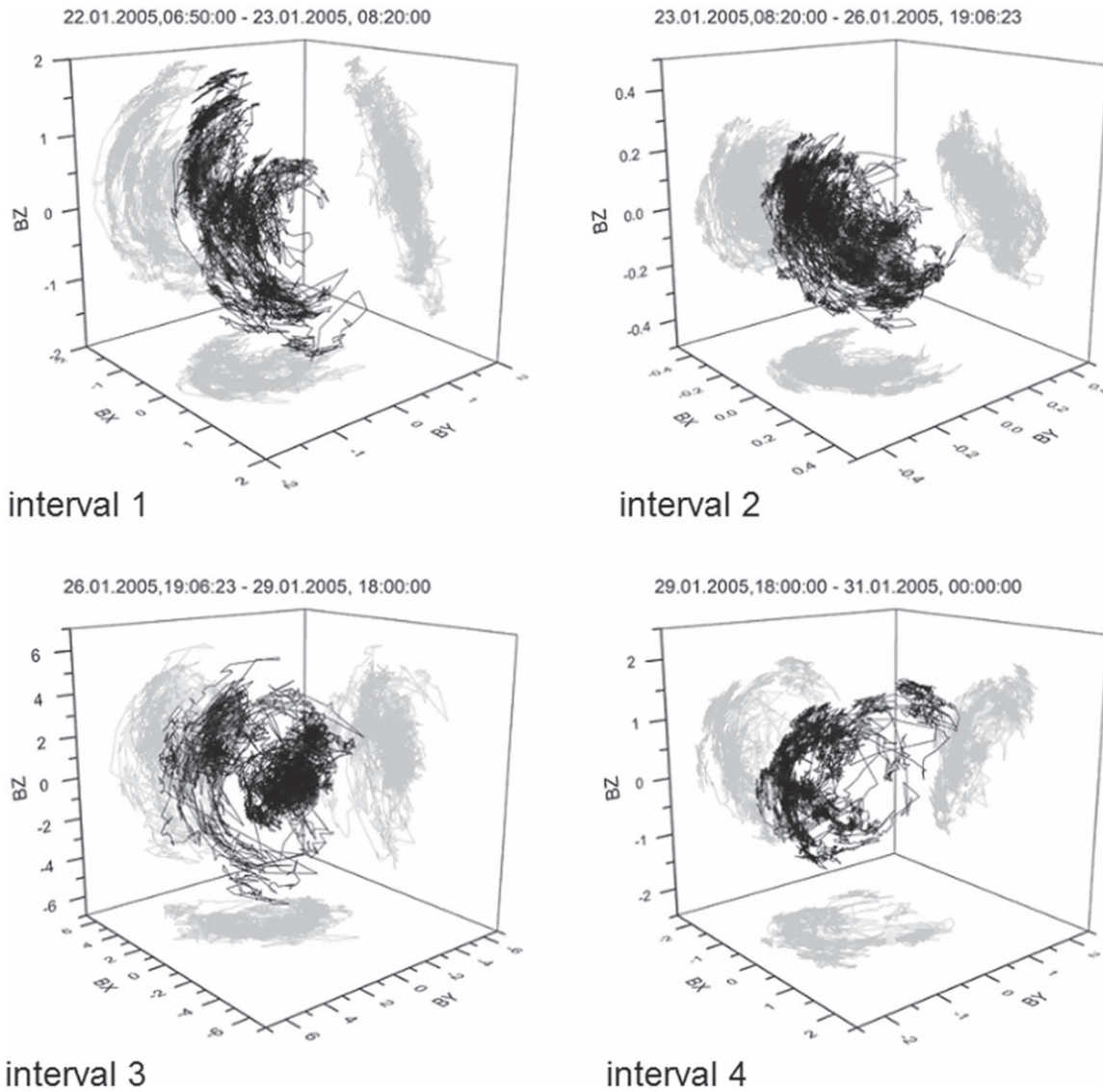
Figure 8. Hodograms of the magnetic field vector in the RTN reference system. Original data have been resampled with a 2 s window. Intervals 2 and 4 do not show large-amplitude arches like intervals 1 and 3. Therefore, signatures of magnetic islands occur mainly in intervals 1 and 3.

previous sections, enhancements in energetic particles flux observed within regions 1 and 3 shown in Figure 5 are not entirely related to SEPs and cannot be associated only with shocks either. Taking into account a possible impact of magnetic islands and CSs on the dynamics of energetic ions, it becomes relevant to study the nature of IMF fluctuations within these four time intervals in order to understand differences that might address the question on the nature of the observed AEPEs.

We find that the whole time period is not particularly Alfvénic, and IMF fluctuations are more likely to occur as a result of advected structures passing across the observation point rather than propagating fluctuations. This conclusion is derived from the observed values of the normalized residual energy σ_r and normalized cross-helicity σ_C shown in Figure 7(a). The normalized residual energy $\sigma_r = (E_V–E_B)/(E_V+E_B)$, where E_V and E_B are kinetic and magnetic energies, respectively, at a given scale (1 hr in our case), is an estimate of the level of energy equipartition. The value of σ_r is expected to be 0 for an Alfvén wave, but it remains generally well below zero throughout the

interval, indicating that these fluctuations at the hourly scale are magnetically dominated.

The bottom panel shows the behavior of the normalized cross-helicity $\sigma_C = (e^+ - e^-)/(e^+ + e^-)$, where e^+ and e^- are the power associated with "inward" and "outward" Alfvénic modes at 1 hr scale, respectively. This parameter would assume values equal to $+1$ or -1 for an inwardly or outwardly propagating Alfvén wave. However, this parameter also confirms the low Alfvénic level of the fluctuations since σ_C fluctuates around quite low values and the dominance of negative values cannot be taken as evidence for "outward"-propagating Alfvénic fluctuations. This is clear evidence for the non-Alfvénic nature of the IMF and plasma fluctuations observed during the entire period of observations. Other processes that may be responsible for the fluctuations include turbulence and magnetic reconnection, both of which are quite possibly related.

The way the IMF direction changes from point to point is known to be a measure of the turbulence strength and is also related to the occurrence of CSs. Figure 7(b) shows histograms
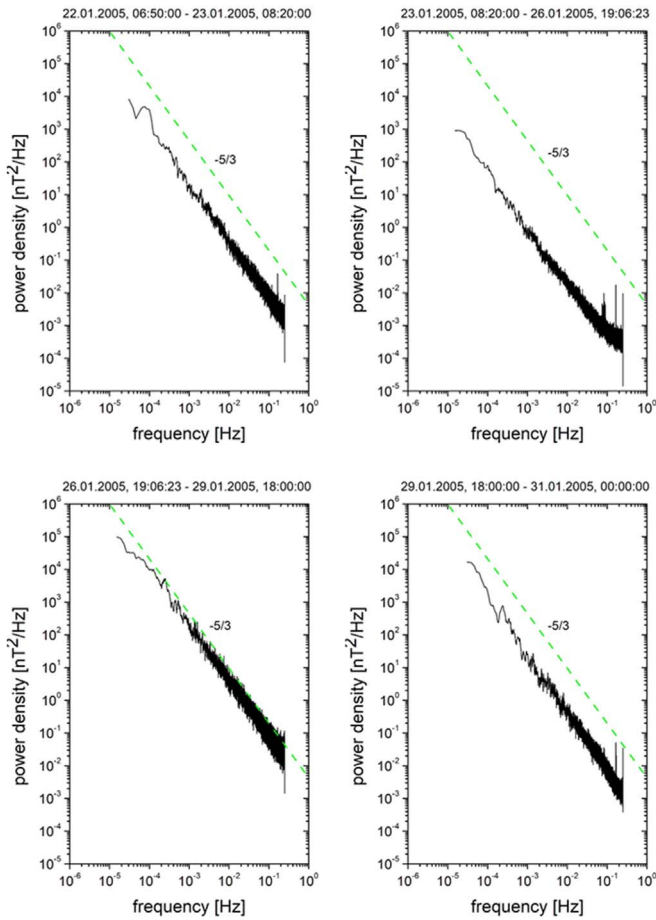
Figure 9. Trace of the power spectral density matrix for each of the four time intervals analyzed. These spectra correspond to intervals 1–4 moving from left to right and from top to bottom. The dashed green line is a reference line indicating the −5/3 Kolmogorov scaling.
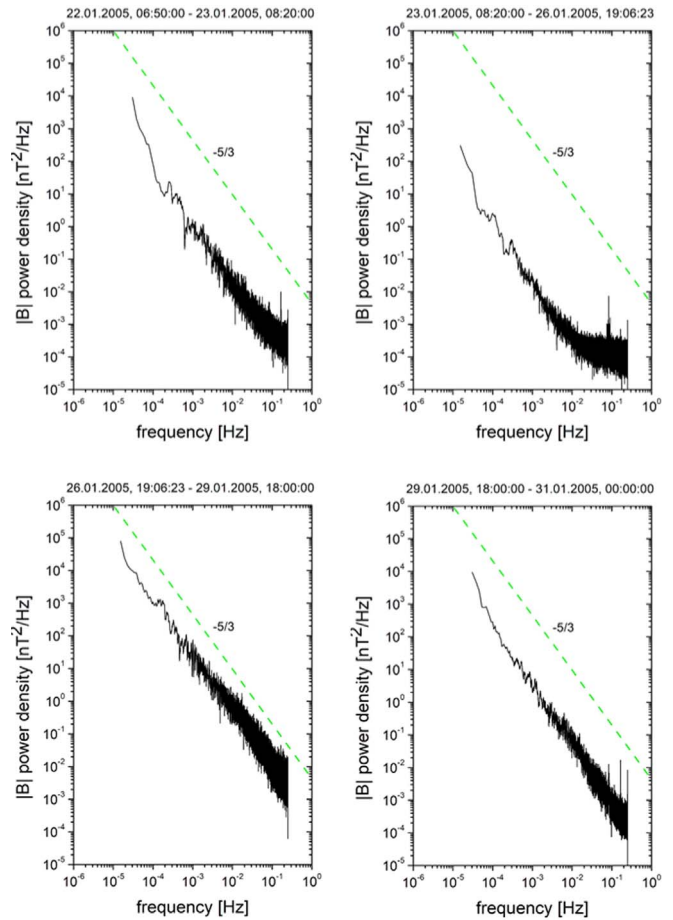

Figure 10. Power spectral density of magnetic field intensity fluctuations for each of the four time intervals analyzed. These spectra correspond to intervals 1 to 4 moving from left to right and from top to bottom. The dashed green line corresponds to a −5/3 Kolmogorov scaling.

of the angle between two successive magnetic field vectors for the four different time intervals. Each histogram has been normalized to the total number of occurrences.

Intervals 2 and 4 are characterized by a smaller relative number of large angular jumps than those observed within intervals 1 and 3 as evident from the figure. Intervals 1 and 3 show the largest directional jumps, with angles roughly larger than 20°.

Additional information on the nature of turbulence in each time interval can be inferred from the topology of the magnetic field vector fluctuations. In Figure 8 we show the location of the tip of the magnetic field vector in the usual RTN reference system for each of our four time intervals. There are clear differences between them. For instance, intervals 1 and 3 show clear large-amplitude arches, roughly suggesting a 2D geometry, which might be the effect of local CS crossings as shown by Bruno et al. (2001). Obviously, the different curvature radii depend on different magnetic field intensities. This is much more evident for interval 3, where the magnetic field undergoes noticeable changes throughout the time interval. The dark *cocoon* identifiable around the center of the reference system of interval 3 is due mainly to the initial and final part of the interval and does not show a clear arch-type configuration, suggesting a less-structured field topology at the borders of the region of interest.

Additional differences in the intervals related to magnetic field fluctuations can be inferred from the spectral analysis as shown in Figure 9. The four panels show the power spectral density (PSD) versus frequency in the spacecraft reference frame for each of the four time intervals. These spectra were obtained from the trace of the spectral density matrix.

The original 2 s magnetic field components and field intensity were first linearly detrended and successively fast Fourier transformed to build the trace of the spectral matrix, which we smoothed using a seven-point running window. The spectra presented in Figure 9 correspond, by definition, to the total spectrum, which involves power due to vector intensity fluctuations plus power due to vector direction fluctuations.

All four spectra indicate that we are dealing with well-developed turbulence since their spectral indices well agree with the typical Kolmogorov index of −5/3 shown for reference in each panel by the green dashed line. Some spectra still show some effect of the spacecraft spin modulation (5 RPM) recognizable as a small peak at ∼0.08 Hz and at several successive harmonics. However, given the small amplitude, the peak is not relevant for the present analysis.

The most pronounced difference between the four spectra is the PSD level, which changes quite remarkably from one interval to the next. The lowest power is associated with fluctuations present in interval 2. In this case, since the power level is so low, the high-frequency part of the spectrum flattens
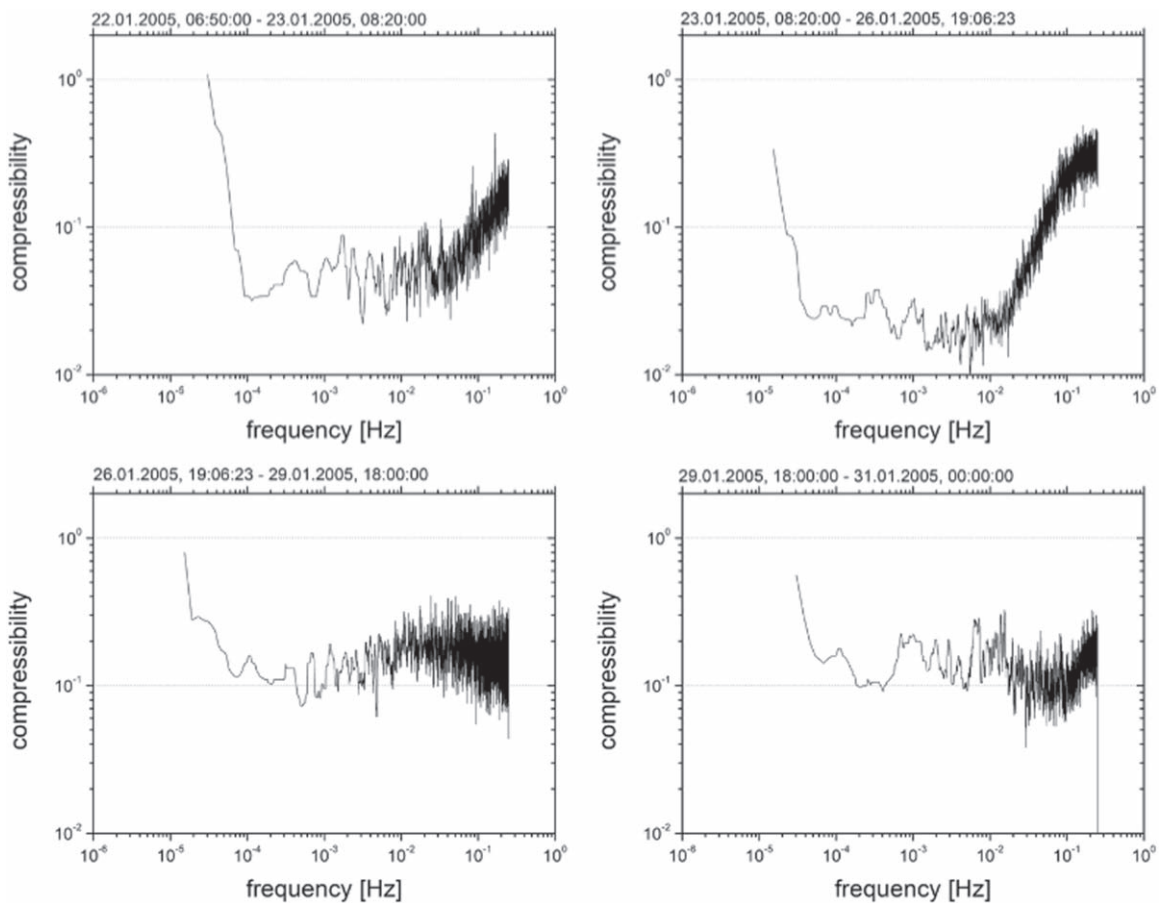
Figure 11. Magnetic field compressibility for each of the four time intervals analyzed. The panels correspond to intervals 1–4 moving from left to right and from top to bottom.
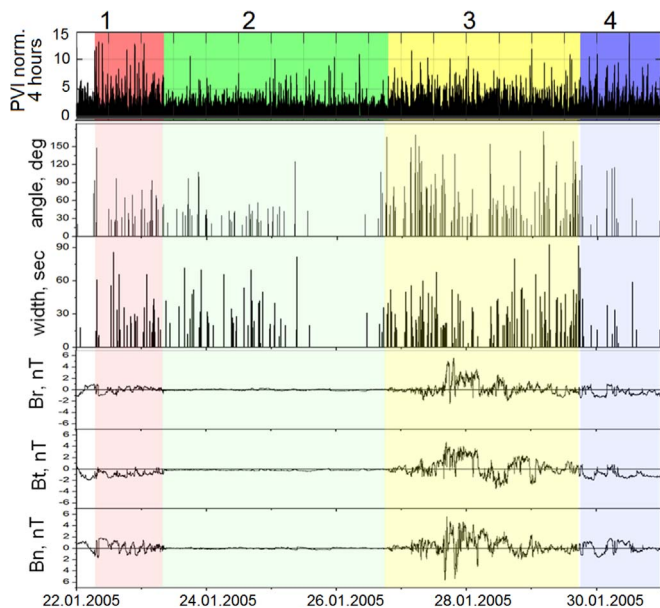

Figure 12. Small-scale coherent structures observed within the four intervals detected with the PVI and CS identification methods. From top to bottom: PVI index normalized over a correlation length (4.4 hr); the angle of the local IMF rotation at a CS crossing in degrees; the CS width in seconds, with the three components of the IMF in the RTN coordinate system.

most probably because the spectral density values are too close to the noise level of the instrument, which is between 1.E-5 and 1.E-4 nT^2/Hz (Balogh et al. 1992). In other words, within this high-frequency range, the white noise generated by the instrument dominates on the real signal. Finally, we observe the highest power level within interval 3, while the spectra of the remaining intervals 1 and 4 are at roughly the same level.

In Figure 10 we show power spectra for fluctuations related only to the magnetic field vector intensity $|B|$. This kind of fluctuations, by definition, can be equal to or less than the total spectrum defined above. Figure 10 is in the same format as Figure 9. As before, interval 3 shows the highest level of fluctuations, while interval 1 and especially interval 2 show the lowest. In addition, since the intensity fluctuation power level is lower than that associated with the trace of the spectral matrix (by definition), the spectrum of interval 2 is more affected by instrumental noise as shown by the strong flattening that extends for about one decade at high frequency.

The compressibility of magnetic fluctuations can be estimated, defined as the ratio of the field intensity spectrum over the trace of the spectral matrix, within the four different regions. The results shown in Figure 11 require a word of caution. In particular, the large increase in compressibility at high frequencies shown in the top panels is an instrumental effect due to noise affecting the high-frequency range of the
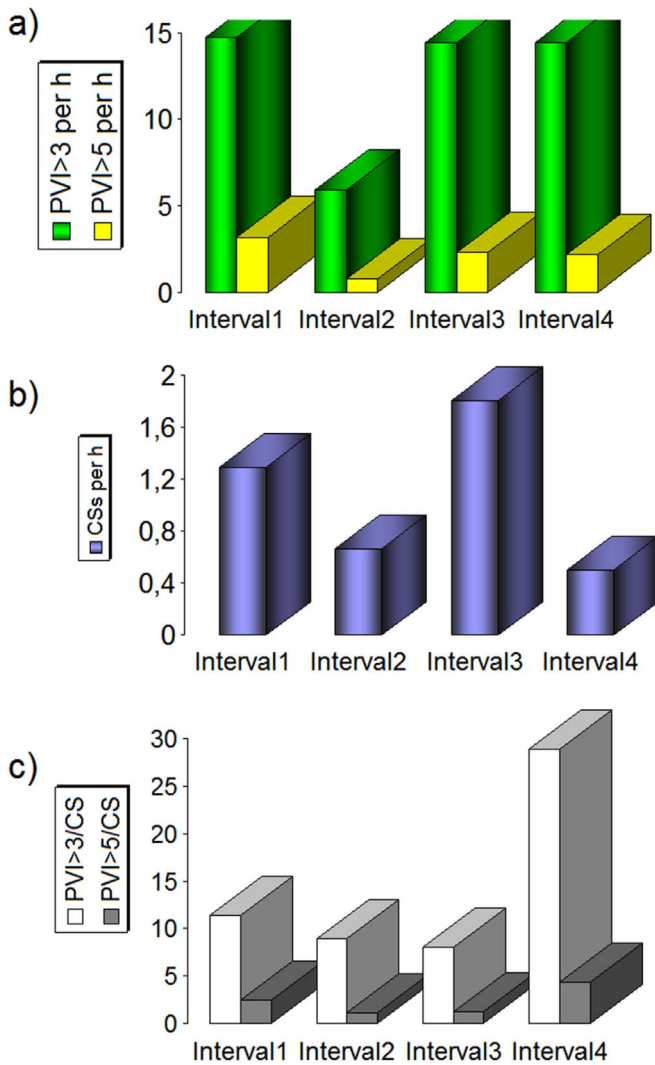
Figure 13. Statistics of PVI events and CSs within the four intervals. (a) Number of PVI events >3 (green) and >5 (yellow) per hour calculated for each interval. (b) Number of CSs per hour calculated for each interval. (c) The ratio of the PVI number to the CS number for PVI events >3 and >5 in white and gray, respectively.

magnetometer and causing the flattening observed in the previous figure. Thus, we do not consider this part of the graphs in the top panels. The compressibility level of interval 2 is the lowest, whereas intervals 3 and 4 indicate a strong increase in compressibility. Interval 3 is the most compressible, and compressibility increases from lower to higher frequency.

In summary, the IMF variations in region 3 suggest the dominant impact of advected, non-Alfvénic structures characterized by larger-amplitude fluctuations and magnetic field rotations in pressure balance conditions, which supports the idea that these IMF fluctuations result from the occurrence of magnetic islands and CSs. Less clear is the situation for interval 1, which shows also some similarities with interval 4. However, in terms of rotational angular width, interval 1 and interval 3 have the largest relative number of events characterized by large rotations above 20° (see Figure 7(b)), supporting the same conclusions already drawn for interval 3.

The other signature of the presence of SMIs is observations of the CSs separating them. Figure 12 illustrates this with an analysis of the IMF variations through the PVI method and the CS identification method, both described in Section 2. The PVI

index is calculated using a time lag corresponding to a scale of ~10 ion inertial lengths, which is chosen since we are focusing on small-scale structures. The PVI is normalized over a correlation length (4.4 hr). The upper PVI panel of Figure 12 shows the presence of coherent structures of all possible origins. Some of them are CSs, but some of them are discontinuities of any sort, including shocks. There is no big difference between the four regions according to this analysis. The CS-only characteristics derived from the CS identification method (Li 2008) are shown in the second and third panels. The occurrence rate of CSs in regions 1 and 3 is higher than in other regions, although they are present in regions 2 and 4 too. The CS angles are larger in region 3, which indicates larger changes in the local IMF direction in this region, which is consistent with our turbulence analysis. To illustrate the increasing CS production in regions 1 and 3, we calculate the CS occurrence rate (see Figure 13).

Figure 13(a) shows the number of PVI events for each interval, where a PVI event is defined as a period where the PVI index is above a certain threshold. The number is calculated per hour to normalize it for the length of the interval. The same normalization is done for the CS number (Figure 13(b)). The ratio of the PVI event number to the CS number for each interval is shown in Figure 13(c). According to Figure 13(a), the number of high PVI events is approximately the same for the first, third, and fourth intervals. There is a decrease within the second (quiet) interval. At the same time, the number of CSs per hour is much higher within the first and third (turbulent) intervals, possibly indicating the intensified formation of SMIs separated by thin CSs detected using Gang Li's method (Li 2008). The relative PVI rate over the CS rate is smallest in the third interval and largest in the fourth interval, which means that the role of CSs, compared to other coherent structures, increases in the turbulent ICME sheath and is insignificant in the main body of the particular ICME.

An additional analysis can be done to confirm the presence of well-shaped magnetic islands within the regions of interest. A GS reconstruction of the spatial profile of local magnetic fields is a very popular technique that, when applied to the solar wind, allows finding a form and specific properties of magnetic islands (Zheng & Hu 2018). Figure 14 shows randomly selected magnetic islands observed within regions 1 (Figure 14(a)) and 3 (Figure 14(b)). In each plot, the magnetic field vector along the spacecraft path is marked by white arrows, the isopotential lines of the potential vector A are shown by the black contours, and the white circle represents the maximum of the Bz component of the local magnetic field. A typical size of magnetic islands can be estimated through the corresponding values in the X- and Y-directions. In the left panels, we show relatively large-scale single islands observed in both intervals. At the same time, there are smaller-scale magnetic islands with clear signatures of their dynamical interaction with surrounding islands and formation of small-scale CSs between them (shown in the right panels). In the two right panels, one can suggest that a process of merging of two magnetic islands (top right panel) and three magnetic islands (bottom right panel) of different sizes is going on. Similarly to laboratory experiments (Furno et al. 2005; Gekelman et al. 2012, 2016, 2018) and observations in the 1 au plasma (Khabarova et al. 2015a, 2015b), bigger islands "swallow" smaller ones while merging. Details of the particular GS reconstructions can be found in Appendix A.
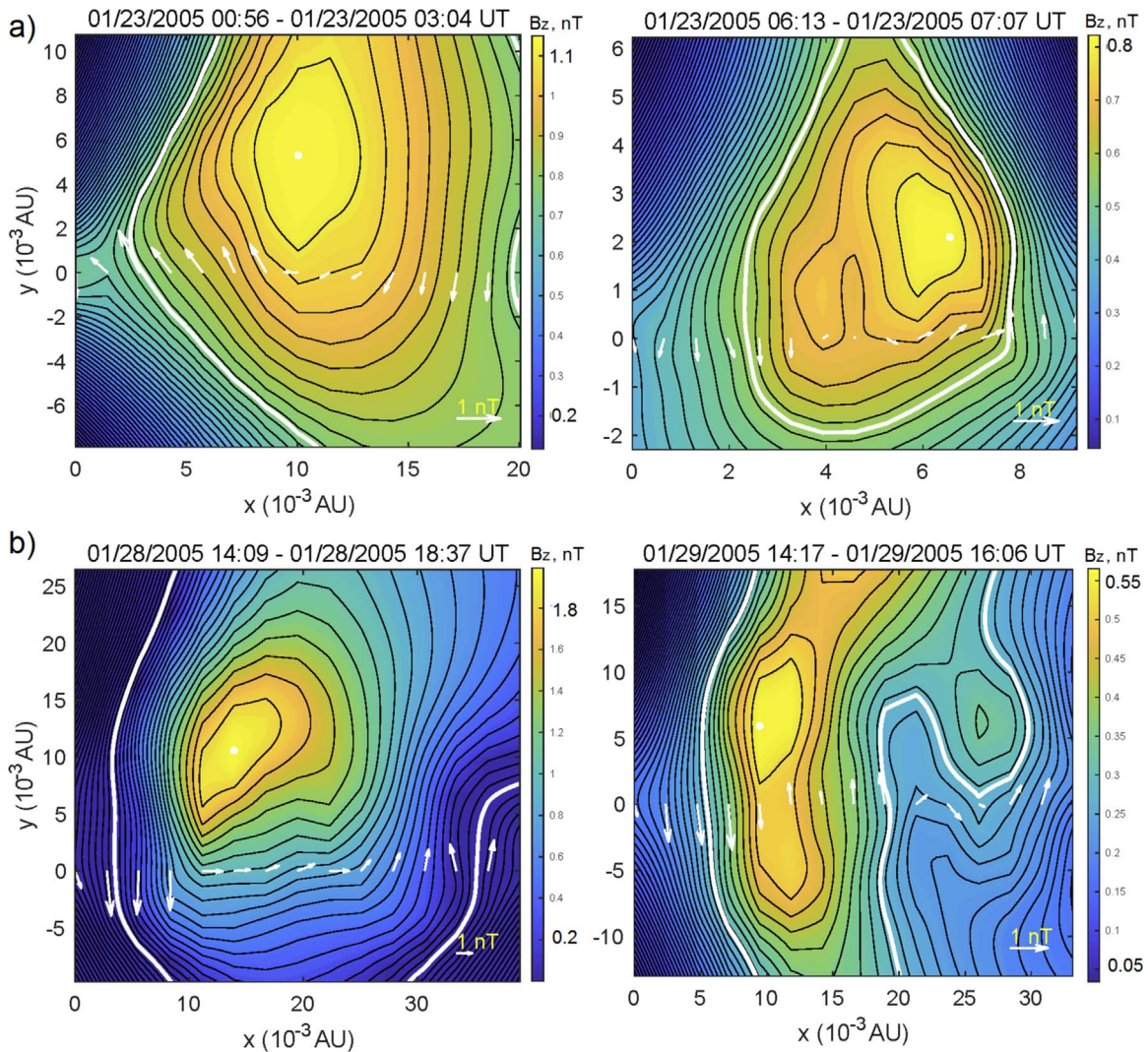
Figure 14. Cross-section maps of the local magnetic field obtained with the Grad–Shafranov technique. Selected magnetic islands are shown for (a) interval 1 and (b) interval 3. The white contour line indicates the flux rope boundary.

Details of the particular GS reconstructions, such as the flux rope list, the corresponding time ranges, sizes, and the transverse pressure as a function of the potential vector A for the selected four intervals, can be found in the supplement (see the List.xlsx file).

Therefore, the analysis above allows us to conclude that IMF variations in regions 1 and 3 are determined predominantly by the occurrence of SMIs separated by small-scale CSs and confined within magnetic cavities formed by shocks and ICME internal SCSs (like the SCS separating the ICME sheath from its main body). Such conditions are known to be favorable for particle confinement and local combined reacceleration in the solar wind.

4. Summary and Discussion

The idea of a possible impact of local structures and dynamical processes on particle transport and acceleration in the heliosphere is not new, but it has recently attracted keen attention of plasma physicists owing to impressive results of modern simulations of the particle behavior in astrophysical plasmas and because of the opportunity to interpret observations more convincingly than before. In particular, complementary

particle energization associated with dynamical processes and magnetic reconnection in magnetic islands is confirmed in both simulations (Guo et al. 2014, 2015, 2016a, 2016b; Zank et al. 2014, 2015a, 2015b; le Roux et al. 2016, 2018a, 2018b; Li et al. 2017, 2018a, 2018b; Du et al. 2018; Zhao et al. 2018; Adhikari et al. 2019; Mingalev et al. 2019) and observations (Khabarova et al. 2015a, 2015b, 2016, 2017, 2018; Zank et al. 2015a; Khabarova & Zank 2017).

A study of the nature of AEPEs with the energetic ion flux increases up to several MeV has been performed earlier for in situ data from 1 au spacecraft, including *ACE*, *Wind*, *STEREO*, and *STEREO B* (see the corresponding references in the Introduction). Although a similar analysis of *Voyager 2* data allowed us to conclude that the local particle acceleration in the solar wind related to dynamical magnetic islands trapped within magnetic cavities took place in the outer heliosphere as well (Zank et al. 2015a; Khabarova et al. 2016, 2017), it was not clear how local particle energization occurs at distances of several astronomical units. We have presented here a detailed analysis of *Ulysses* observations of AEPEs at ∼5 au near the ecliptic plane, discussing the role of local particle acceleration in the whole picture of observed AEPEs.

15

We should note that it is impossible to find a direct confirmation that observed AEPEs are related to dynamical processes in SMIs since the mechanism of particle acceleration is based on collective effects. Although there is some modulation of the energetic particle flux profile corresponding to crossings of borders of SMIs, one cannot trace particles from numerous reconnecting sites. There are two ways to show the correspondence between AEPEs and SMIs. One may either model characteristics of AEPEs or show a chain of accompanying phenomena that should be observed according to theoretical predictions. The first approach has recently been employed by Zhao et al. (2018) and Adhikari et al. (2019), and here we use the second.

A logical string of the study is as follows:

(1) We present the behavior of energetic ion fluxes over all energy channels as observed by the HI-SCALE instrument onboard *Ulysses*.

(2) We show that there are periods of strange mismatches between time–intensity profiles of the lower- and higher-energy ion flux, i.e., there are signatures of additional particle acceleration of lower-energy ions seen as hump-like enhancements in lower-energy channels on top of the smooth higher-energy profiles.

(3) Taking into account our previous studies on local sources of particle energization, we analyze IMF variations and show that there is a big difference between the IMF/plasma properties within and out of the AEPE periods, and the difference is determined by the dominance of SMIs and CSs separating them. We additionally present evidence for the presence of magnetic islands within the time intervals of our particular interest, employing the GS technique.

The key results obtained in the study can be summarized as follows:

1. In the event studied above, energetic ion flux enhancements in lower-energy channels have a profile considerably different from higher-energy channels. We conclude that energetic particle flux enhancements up to ∼0.6 MeV are mostly determined by local particle acceleration occurring in regions filled with SMIs and CSs.
2. We prove that the variations in the IMF observed in these regions are not associated with Alfvénic fluctuations; therefore, the corresponding AEPEs cannot be explained simply by a wave activity or large-scale turbulence. The number of CSs is predominantly higher in regions where the AEPEs are observed, and the IMF vector rotates in the same regions. The restoration of the IMF spatial profile with the GS technique also shows SMIs in the regions.
3. We found that AEPEs downstream of the merged ICME shock are characterized by the flux amplification factor exceeding 1, which points to the existence of a mechanism of particle acceleration apart from DSA. The AEPEs cannot be explained by connection to the shock, as they are observed several correlation lengths apart, i.e., too far from the shock to allow particles to come back. Furthermore, the regions in which the AEPEs are observed are separated from the shock by several SCSs, preventing free propagation of accelerated particles further downstream. The AEPEs observed deep inside the 5.2 au ICME cannot be interpreted as an additional ejection of particles from a coronal source either. Therefore, although the scenario of the "connection

issue" cannot necessarily be ruled out, it cannot be ruled in either in this particular event.
4. Considering all the results together, we conclude that local particle acceleration in the regions is governed not only by shocks but also by dynamical magnetic islands and stochastically reconnecting CSs.

We provide a possible interpretation of the event, bringing all facts together and suggesting the coexistence of different sources of accelerated particles in the solar wind that may contribute to observed profiles of the energetic particle flux at different energies. Additionally to the well-known effect of simultaneous observations of preexisting SEPs and energetic particles accelerated locally by interplanetary shocks via DSA, we show that one more local source of particle energization may occur, which is dynamical processes in magnetic islands and CSs (as described by Zank et al. 2014, 2015a, 2015b; le Roux et al. 2015, 2016, 2018a, 2018b).

The obtained results allow us to assume that this particular event is an example of the confinement and effective reacceleration of energetic particles that occurs within a natural analog of a tokamak in the solar wind (as previously discussed in Khabarova et al. 2016, 2017, 2018). Beyond Earth, a situation when an ICME is squeezed by a CIR in one direction and by overtaking ICME in the other direction is very typical. Consequently, seed particles such as SEPs and DSA particles may be both trapped inside magnetic islands and larger magnetic cavities (i.e., boundaries of the streams and their main internal parts) and contribute in the formation of time–intensity profiles of the energetic ion flux. Without the confinement, energetic particles would propagate freely, classically, as higher-energy solar energetic particles with energies above 5 MeV do in the event studied here, and those enhancements and variations in the energetic ion flux at lower energies would not be observed.

A specific point discussed in several papers (e.g., Desai et al. 1999; Chotoo et al. 2000; Tsubouchi 2011) was a peak (or several enhancements) of the low-energy ion flux inside CIRs, between the SI and the RS, similarly to what is observed in region 1 in Figure 5. A shock-related explanation is usually given for such events. We would like to note that another mechanism contributing to the observed picture of the energetic ion flux enhancements may be suggested. As an example, we show the event from Chotoo et al. (2000) revisited in terms of the occurrence of SCSs and magnetic islands formed in the turbulent area between the SI and the RS (see Appendix B). One can easily find that there is a clear crossing of SCSs inside the region downstream of the reverse shock (region 1). A simple analysis of the behavior of the IMF components in the region of interest also shows that there is a clear rotation of the IMF vector, which, in combination with the occurrence of SCSs, suggests the occurrence of magnetic islands. Therefore, pure DSA effects may be enhanced by an additional local particle acceleration operating in dynamical magnetic islands, according to the mechanism proposed by Zank et al. (2014, 2015a) and le Roux et al. (2015, 2016, 2018a).

Summarizing, we show that local coherent structures in the solar wind such as magnetic islands and CSs may not only modulate time–intensity profiles of energetic ion flux but also effectively contribute to particle acceleration in the heliosphere. The latter is important for understanding of particle transport in the heliosphere, including the propagation of cosmic rays (Engelbrecht 2019), and allows considering the discussed

phenomena as a still insufficiently investigated manifestation of changing space weather.

Appendix A
Details of the Grad–Shafranov Reconstruction of Magnetic Islands

Plots of the transverse pressure P_t as a function of the potential vector A and the corresponding fits are shown in Figure 15 to verify the double-folding behavior, which ensures a meaningful Grad–Shafranov reconstruction. The criteria of the reconstruction are the same as in Chen et al. (2018). The limits of the fitting residue (less than 0.14) and the difference residue (less than 0.12) are applied to identify small-scale flux
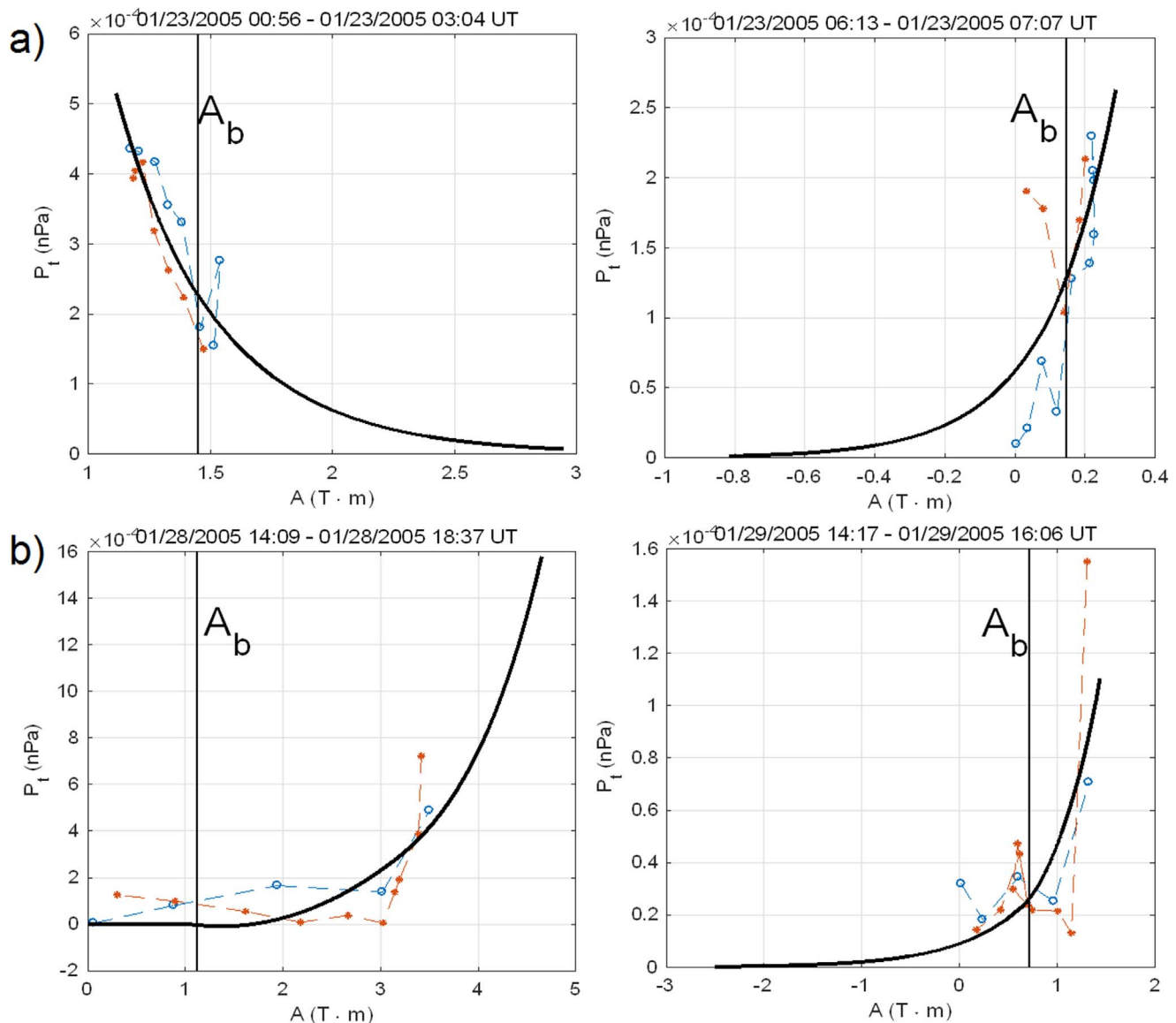
Figure 15. Fitting curves (solid black lines) of P_t versus A are plotted for the corresponding color maps of Figure 14. Vertical black line A_b denotes the flux rope boundary. Two branches of the double-folding pattern are shown as red dots and blue circles.

ropes. Panels of Figure 15 correspond to the four panels of Figure 14.

Appendix B
On the Nature of Energetic Particle Enhancements in the Region Between a CIR Stream Interface and a Reverse Shock

The region between a CIR stream interface (SI) and a reverse shock (RS) (we will call it region 1, following Figure 5 of the manuscript) is a turbulent region similar to the turbulent ICME sheath observed between a forward shock (FS) and the main body of an ICME. Since RSs propagate in the sunward direction, and FSs in the opposite, anti-sunward direction, region 1 is downstream of the shock. In the context of in situ observations, this means that the main effects of DSA are seen before the crossing of a RS, similarly to those observed behind a FS.

Properties of CIR-associated energetic ion flux enhancements observed in keV–MeV channels in region 1 are often attributed entirely to the diffusive shock acceleration (DSA) interpretation. However, in some events, it is not that easy to interpret them within a classic DSA paradigm since the lower-energy time–intensity profiles do not follow the higher-intensity ones, and some additional prominent peaks are observed in lower-energy channels in region 1 instead of the expected rather smooth decrease with respect to the position of the shock. Taking into account a possibility of additional

mechanisms of local particle acceleration operating in region 1, it is reasonable to revisit such events, looking for signatures of coherent structures in the region of interest.

As an example, we present below a quick analysis of the CIR1 event shown in Chotoo et al. (2000), focusing on the existence of magnetic islands within interval 1 in which unusual enhancements in low-energy channels were observed downstream of the fast RS that was detected by the Wind spacecraft on April 7, 1995 at 20:26:09 UT. Figure 16(a) represents a combination of Figure 2 and Figure 3 from Chotoo et al. (2000) to illustrate the behavior of the IMF vector. The yellow stripe in Figure 16(a) indicates region 1. It is known that typical DSA-associated profiles always peak at the shock position. The fact that CIR-associated peaks can sometimes be observed inside region 1 is the first signature of a possible contribution of a mechanism additional to DSA.

A re-examination of the event shows the following:

(1) There is a clear crossing of strong current sheets inside region 1 downstream of the reverse shock, according to the characteristic IMF variations observed. One can see the corresponding changes in the S+/N− polarity in Figure 16(a), the rotation of the IMF in the vertical direction according to changes in the clock angle B_θ, and the deep decrease in the IMF strength typical for the crossing of a strong current sheet, which is shown by the vertical red dashed line. Additionally, a local increase in the solar wind speed and temperature (not shown) may
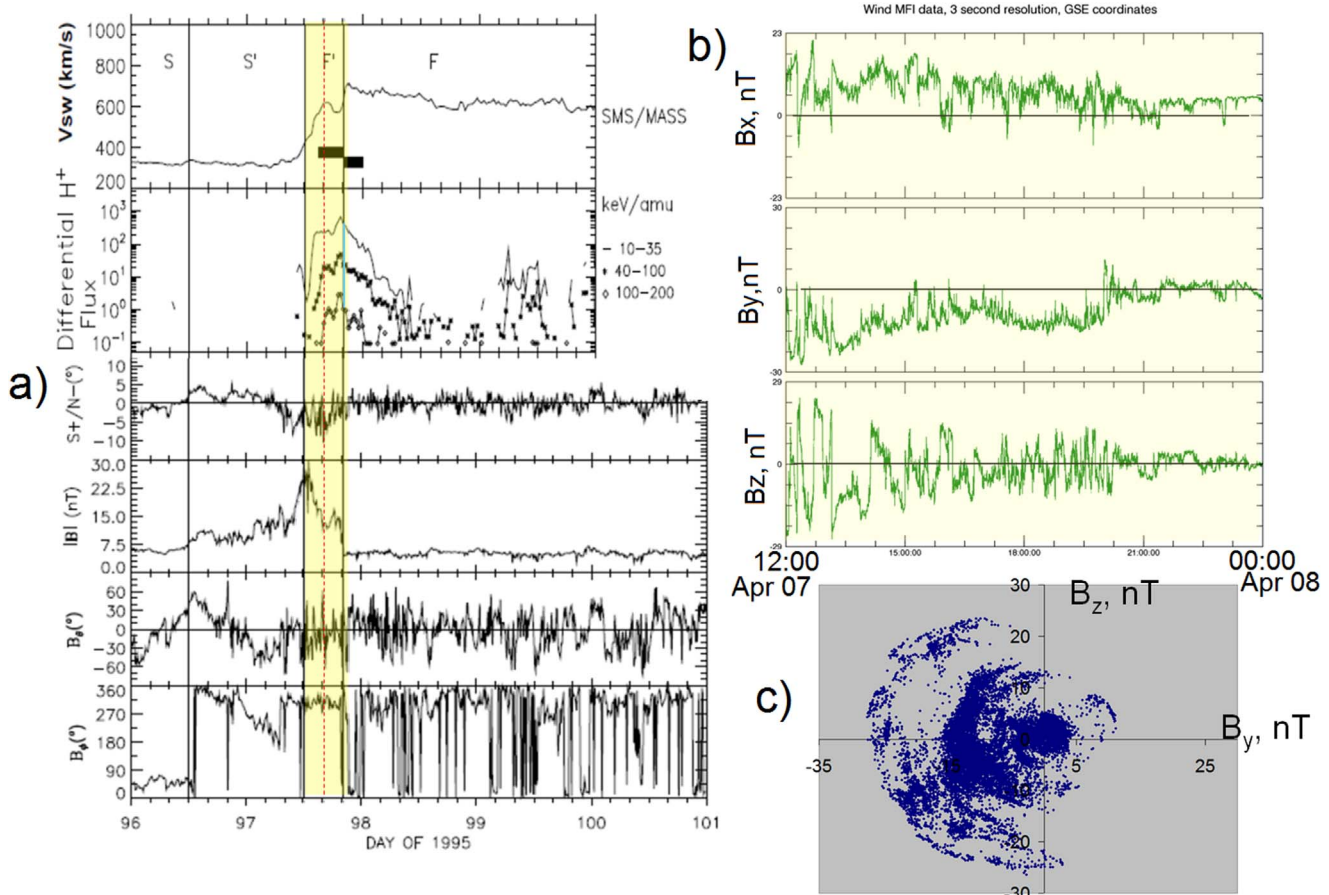

Figure 16. Additional analysis of the IMF variations in region 1 of CIR1 previously discussed by Chotoo et al. (2000). (a) Yellow stripe (to the left with regard to the shock) indicates the interval within which an AEPE is observed, and the red dash line shows the crossing of the strongest current sheet within turbulent region 1 downstream of the RS; (b) Variations in the three IMF components within the interval of interest; (c) Rotation of the IMF vector in the Bz-By plane within region 1.

indicate the ongoing magnetic reconnection. The lower-energy ion flux curves show more prominent enhancements than higher-energy ones that peak at the shock.

(2) A simple analysis of the behavior of the IMF vector in the region of interest (Figure 16(b)) shows variations in the IMF components typical for the presence of magnetic islands separated by current sheets. Indeed, there is a clear rotation of the IMF vector in the Bz-By plane as shown in Figure 16(c), which is usually considered as a strong evidence for the occurrence of magnetic islands.

Therefore, the explanation provided by Chotoo et al. can be enhanced if one suggests a possibility of additional local particle acceleration operating in compressed and dynamical magnetic islands in region 1 according to the mechanism proposed by Zank et al. (2014).

ORCID iDs

Olga Malandraki ● https://orcid.org/0000-0002-4751-6835
Olga Khabarova ● https://orcid.org/0000-0002-3230-2033
Roberto Bruno ● https://orcid.org/0000-0002-2152-0115
Gary P. Zank ● https://orcid.org/0000-0002-4642-6192
Gang Li ● https://orcid.org/0000-0003-4695-8866
Bernard Jackson ● https://orcid.org/0000-0001-7664-5858
Mario M. Bisi ● https://orcid.org/0000-0001-6821-9576
Antonella Greco ● https://orcid.org/0000-0001-5680-4487
Oreste Pezzi ● https://orcid.org/0000-0002-7638-1706
William Matthaeus ● https://orcid.org/0000-0001-7224-6024
Alexandros Chasapis Giannakopoulos ● https://orcid.org/0000-0001-8478-5797
Helmi Malova ● https://orcid.org/0000-0001-6511-2335
Roman Kislov ● https://orcid.org/0000-0002-5609-7572
Frederic Effenberger ● https://orcid.org/0000-0002-7388-6581
Jakobus le Roux ● https://orcid.org/0000-0001-9199-2890
Yu Chen ● https://orcid.org/0000-0002-0065-7622
Qiang Hu ● https://orcid.org/0000-0002-7570-2301
N. Eugene Engelbrecht ● https://orcid.org/0000-0003-3659-7956

References

Adhikari, L., Khabarova, O., Zank, G. P., & Zhao, L.-L. 2019, ApJ, 873, 72
Alexandrova, O., Carbone, V., Veltri, P., & Sorriso-Valvo, L. 2008, ApJ, 674, 1153
Al-Sawad, A., Saloniemi, O., Laitinen, T., & Kocharov, L. 2009, A&A, 497, L1
Ambrosiano, J., Matthaeus, W. H., Goldstein, M. L., & Plante, D. 1988, JGR, 93, 14383
Antiochos, S. K., Mikić, Z., Titov, V. S., Lionello, R., & Linker, J. A. 2011, ApJ, 731, 112
Axford, W. I., Leer, E., & McKenzie, J. F. 1982, A&A, 111, 317
Balogh, A., Beek, T. J., Forsyth, R. J., et al. 1992, A&AS, 92, 221
Battarbee, M., Dalla, S., & Marsh, M. S. 2017, ApJ, 836, 138
Bell, A. R. 1978a, MNRAS, 182, 147
Bell, A. R. 1978b, MNRAS, 182, 443
Bian, N. H., & Kontar, E. P. 2013, PhRvL, 110, 151101
Bisi, M. 2016, in Heliophysics: Active Stars, Their Astrospheres, and Impacts on Planetary Environments, ed. C. Schrijver, F. Bagenal, & J. Sojka (Cambridge: Cambridge Univ. Press), 289
Bisi, M. M., Jackson, B. V., Breen, A. R., et al. 2010, SoPh, 265, 233
Bisi, M. M., Jackson, B. V., Hick, P. P., et al. 2008, JGR, 113, A00A11
Bruno, R., & Carbone, V. 2013, LRSP, 10, 208, 1
Bruno, R., Carbone, V., Veltri, P., Pietropaolo, E., & Bavassano, B. 2001, P&SS, 49, 1201
Buffington, A., Bisi, M. M., Clover, J. M., et al. 2008, ApJ, 677, 798

Buffington, A., Bisi, M. M., Clover, J. M., et al. 2009, Icar, 203, 124
Burlaga, L. F., McDonald, F. B., & Schwenn, R. 1986, JGR, 91, 331, 13
Cartwright, M. L., & Moldwin, M. B. 2010, JGR, 115, A08102
Chen, Y., Hu, Q., le Roux, J., & Zheng, J. 2018, J. Phys. Conf. Ser., 1100, 012006
Chollet, E. E., Mewaldt, R. A., Cummings, A. C., et al. 2010, JGR, 115, A12106
Chotoo, K., Schwadron, N. A., Mason, G. M., et al. 2000, JGR, 105, A10
Cohen, C. M. S., Mason, G. M., Mewaldt, R. A., & Wiedenbeck, M. E. 2014, ApJ, 793, 35
Dahlin, J. T., Drake, J. F., & Swisdak, M. 2017, PhPl, 24, 092110
Dalena, S., Rappazzo, A. F., Dmitruk, P., Greco, A., & Matthaeus, W. H. 2014, ApJ, 783, 143
DeForest, C. E., Howard, T. A., & McComas, D. J. 2012, ApJ, 745, 36
Desai, M. I., & Giacalone, J. 2016, LRSP, 13, 3
Desai, M. I., Marsden, R. G., Sanderson, T. R., et al. 1999, JGR, 104, 6705
Dmitruk, P., Matthaeus, W. H., & Seenu, N. 2004, ApJ, 617, 667
Drake, J. F., Opher, M., Swisdak, M., & Chamoun, J. N. 2010, ApJ, 709, 963
Drake, J. F., Swisdak, M., Che, H., & Shay, M. A. 2006, Natur, 443, 7111, 553
Drake, J. F., Swisdak, M., & Fermo, R. 2013, ApJL, 763, L5
Dresing, N., Gómez-Herrero, R., Heber, B., et al. 2014, A&A, 567, A27
Du, S., Guo, F., Zank, G. P., Li, X., & Stanier, A. 2018, ApJ, 867, 16
Engelbrecht, N. E. 2019, ApJ, 872, 124
Eyles, C. J., Simnett, G. M., Cooke, M. P., et al. 2003, SoPh, 217, 319
Fermo, R. L., Opher, M., & Drake, J. F. 2014, PhRevL, 113, 031101
Fisk, L. A., & Gloeckler, G. 2012, SSRv, 173, 433
Fisk, L. A., & Gloeckler, G. 2014, JGR, 119, 8733
Forsyth, R. J., & Marsch, E. 1999, SSRv, 89, 7
Foullon, C., Lavraud, B., Luhmann, J. G., et al. 2011, ApJ, 737, 16
Furno, I., Intrator, T. P., Hemsing, E. W., et al. 2005, PhPl, 12, 055702 5
Gary, S. P., Saito, S., & Narita, Y. 2010, ApJ, 716, 1332
Gekelman, W., De Haas, T., Daughton, W., et al. 2016, PhRvL, 116, 235101
Gekelman, W., DeHaas, T., Pribyl, P., et al. 2018, ApJ, 853, 33
Gekelman, W., Lawrence, E., & Van Compernolle, B. 2012, ApJ, 753, 131
Gómez-Herrero, R., Dresing, N., Klassen, A., et al. 2015, ApJ, 799, 17
Gonzalez, C. A., Dmitruk, P., Mininni, P. D., & Matthaeus, W. H. 2017, ApJ, 850, 19
Gopalswamy, N., Xie, H., Yashiro, S., et al. 2012, SSRv, 171, 23
Gosling, J. T., McComas, D. J., Skoug, R. M., & Forsyth, R. J. 2001, SSRv, 97, 189
Gosling, J. T., & Pizzo, V. J. 1999, SSRv, 89, 21
Gosling, J. T., Skoug, R. M., Haggerty, D. K., & McComas, D. J. 2005, GeoRL, 32, L14113
Greco, A., Matthaeus, W. H., Perri, S., et al. 2018, SSRv, 214, 1
Guo, F., Li, H., Daughton, W., Li, X., & Liu, Y. H. 2016a, PhPl, 23, 055708
Guo, F., Li, H., Daughton, W., & Liu, Y. H. 2014, PhRvL, 113, 155005
Guo, F., Li, S., Li, H., et al. 2012, ApJ, 747, 98
Guo, F., Li, X., Li, H., et al. 2016b, ApJL, 818, L9
Guo, F., Liu, Y. H., Daughton, W., & Li, H. 2015, ApJ, 806, 167
Hau, L.-N., & Sonnerup, B. U. Ö. 1999, JGR, 104, 6899
Heras, A. M., Sanahuja, B., Lario, D., et al. 1995, ApJ, 445, 497
Hu, Q. 2017, SoPh, 292, 116, 9
Iucci, N., Dorman, L. I., Levitin, A. E., et al. 2006, AdSpR, 37, 184
Jackson, B. V., Bisi, M. M., Hick, P. P., et al. 2008, JGR, 113, A00A15
Jackson, B. V., Buffington, A., Hick, P. P., et al. 2004, SoPh, 225, 177
Jackson, B. V., Buffington, A., Hick, P. P., Wang, X., & Webb, D. 2006, JGR, 111, A04S91
Jackson, B. V., Hick, P. P., Buffington, A., Bisi, M. M., & Clover, J. M. 2009, AnGeo, 27, 4097
Jian, L. K., Russell, C. T., Luhmann, J. G., et al. 2011, SoPh, 273, 179
Jian, L. K., Russell, C. T., Luhmann, J. G., Skoug, R. M., & Steinberg, J. T. 2008, SoPh, 250, 375
Khabarova, O., Zank, G. P., Li, G., et al. 2015a, ApJ, 808, 181
Khabarova, O., Zank, G. P., Li, G., et al. 2015b, JPhCS, 642, 012033
Khabarova, O. V., Malandraki, O. E., Zank, G. P., et al. 2018, in Proc. IAU Symp. 335, Space Weather in the Heliosphere: Processes and Forecasts, ed. C. Foullon & O. Malandraki (Cambridge: Cambridge Univ. Press), 76
Khabarova, O. V., & Zank, G. P. 2017, ApJ, 843, 4, 1
Khabarova, O. V., Zank, G. P., Li, G., et al. 2016, ApJ, 827, 122
Khabarova, O. V., Zank, G. P., Malandraki, O. E., et al. 2017, SunGeo, 12, 23
Lanzerotti, L. J., Gold, R. E., Anderson, K. A., et al. 1992, A&AS, 92, 349
Lario, D., Sanahuja, B., & Heras, A. M. 1998, ApJ, 509, 415
Laurenza, M., Consolini, G., Storini, M., et al. 2016, IOP Conf. Series, JPhCS, 767, 012015
Lazarian, A., Vlahos, L., Kowal, G., et al. 2012, SSRv, 173, 557
le Roux, J. A., Zank, G. P., & Khabarova, O. V. 2018a, ApJ, 864, 158

le Roux, J. A., Zank, G. P., & Khabarova, O. V. 2018b, IOP Conf. Series, JPhCS, 1100, 012015
le Roux, J. A., Zank, G. P., Webb, G. M., & Khabarova, O. 2015, ApJ, 801, 112
le Roux, J. A., Zank, G. P., Webb, G. M., & Khabarova, O. 2016, ApJ, 827, 47
Lee, M. A., & Ryan, J. M. 1986, ApJ, 303, 829
Li, G. 2008, ApJL, 672, L65
Li, G., Miao, B., Hu, Q., & Qin, G. 2011, PhRvL, 106, 125001 12
Li, G., Zank, G. P., & Rice, W. K. M. 2003, JGR, 108, 1082
Li, X., Guo, F., Li, H., & Birn, J. 2018a, ApJ, 855, 80
Li, X., Guo, F., Li, H., & Li, G. 2017, ApJ, 843, 21
Li, X., Guo, F., Li, H., & Li, S. 2018b, ApJ, 866, 4
Malandraki, O. 2015, JPhCS, 632, 012070
Malandraki, O. E., Agueda, N., Papaioannou, A., et al. 2012, SoPh, 281, 333
Malandraki, O. E., & Crosby, N. B. 2018a, in Solar Particle Radiation Storms Forecasting and Analysis, vol. 444 ed. O. E. Malandraki & N. B. Crosby (Cham: Springer International Publishing), 1
Malandraki, O. E., & Crosby, N. B. 2018b, SpWea, 16, 591
Malandraki, O. E., Lario, D., Lanzerotti, L. J., et al. 2005, JGR, 110, A09S06
Malandraki, O. E., Marsden, R. G., Lario, D., et al. 2009, ApJ, 704, 469
Malandraki, O. E., Marsden, R. G., Tranquille, C., et al. 2007, JGR, 112, A06111
Malandraki, O. E., Marsden, R. G., Tranquille, C., et al. 2008, AnGeo, 26, 1029
Manchester, W., IV, & Van Der Holst, B. 2017, JPhCS, 900, 012015
Marhavilas, P. K., Malandraki, O. E., & Anagnostopoulos, G. C. 2015, P&SS, 117, 192
Marsch, E. 2006, LRSP, 3, 1
Matthaeus, W. H., Ambrosiano, J. J., & Goldstein, M. L. 1984, PhRvL, 53, 1449
Miao, B., Peng, B., & Li, G. 2011, AnGeo, 29, 237
Mingalev, O. V., Khabarova, O. V., Malova, K. V., et al. 2019, SoSyR, 53, 30, 1
Miroshnichenko, L. 2015, Solar Cosmic Rays: Fundamentals and Applications (Switzerland: Springer), 405
Mulligan, T., Blake, J. B., Mewaldt, R. A., & Leske, R. A. 2008, in AIP Conf. Proc. 1039, Particle Acceleration and Transport in the Heliosphere and Beyond: 7th Annual Int. Astrophysics Conference, ed. G. Li et al. (New York: AIP), 162
National Research Council 2006, Health Risks from Exposure to Low Levels of Ionizing Radiation: BEIR VII Phase 2 (Washington, DC: National Academies Press), doi:https://doi.org/10.17226/11340

Ng, C. K., Reames, D. V., & Tylka, A. J. 2003, ApJ, 591, 461
Oka, M., Phan, T.-D., Krucker, S., Fujimoto, M., & Shinohara, I. 2010, ApJ, 714, 915
Pallocchia, G., Laurenza, M., & Consolini, G. 2017, ApJ, 837, 158
Pezzi, O., Servidio, S., Perrone, D., et al. 2018, PhPl, 25, 060704
Pritchett, P. L. 2008, PhPl, 15, 102105
Pucci, F., Servidio, S., Sorriso-Valvo, L., et al. 2017, ApJ, 841, 60
Reames, D. V. 1999, SSRv, 90, 413
Rice, W. K. M., Zank, G. P., & Li, G. 2003, JGR, 108, 1369
Richardson, I. G. 2018, LRSP, 15, 1
Richardson, J. D., Wang, C., Kasper, J. C., & Liu, Y. 2005, GeoRL, 32, L03S03
Sahraoui, F., Galtier, S., & Belmont, G. 2007, JPlPh, 73, 723
Servidio, S., Dmitruk, P., Greco, A., et al. 2011, NPGeo, 18, 675
Servidio, S., Matthaeus, W. H., Shay, M. A., et al. 2010, PhPl, 17, 032315
Servidio, S., Matthaeus, W. H., Shay, M. A., Cassak, P. A., & Dmitruk, P. 2009, PhRvL, 102, 115003
Servidio, S., Valentini, F., Perrone, D., et al. 2015, JPlPh, 81, 325810107
Sonnerup, B. U. Ö., & Guo, M. 1996, GeoRL, 23, 3679
Stasiewicz, K., Markidis, S., Eliasson, B., Strumik, M., & Yamauchi, M. 2013, EPL, 102, 49001
Tappin, S. J., Buffington, A., Cooke, M. P., et al. 2004, GeoRL, 31, L2802
Tessein, J. A., Ruffolo, D., Matthaeus, W. H., & Wan, M. 2016, GeoRL, 43, 3620
Trenchi, L., Bruno, R., D'Amicis, R., Marcucci, M. F., & Telloni, D. 2013, AnGeo, 31, 1333
Tsubouchi, K. 2011, ApJ, 740, 115
Tsubouchi, K. 2014, ApJ, 795, 47
Valentini, F., Perrone, D., Stabile, S., et al. 2016, NJPh, 18, 125001
Verkhoglyadova, O. P., Zank, G. P., & Li, G. 2015, PhR, 557, 1
von Rosenvinge, T. T., Richardson, I. G., Reames, D. V., et al. 2009, SoPh, 256, 443
Wang, Y., Zhuang, B., Hu, Q., et al. 2016, JGRA, 121, 9316
Xu, X., Wei, F., & Feng, X. 2011, JGRA, 116, A5
Zank, G. P., Hunana, P., Mostafavi, P., et al. 2015a, ApJ, 814, 137
Zank, G. P., Hunana, P., Mostafavi, P., et al. 2015b, JPhCS, 642, 012031
Zank, G. P., le Roux, J. A., Webb, G. M., Dosch, A., & Khabarova, O. 2014, ApJ, 797, 28
Zank, G. P., Rice, W. K. M., & Wu, C. C. 2000, JGR, 105, 25079
Zhao, L.-L., Zank, G. P., Khabarova, O., et al. 2018, ApJL, 864, L34
Zharkova, V. V., & Khabarova, O. V. 2015, AnGeo, 33, 457
Zheng, J., & Hu, Q. 2018, ApJL, 852, L23